The Astrophysical Journal, 952:17 (22pp), 2023 July 20 https://doi.org/10.3847/1538-4357/acdb4a

Understanding the Molecular Kinetics and Chemical Equilibrium Phase of Frozen CO during Bombardment by Cosmic Rays by Employing the PROCODA Code

S. Pilling[1], G. A. Carvalho[1,2], H. A. de Abreu[3], B. R. L. Galvão[4], C. H. da Silveira[1], and M. S. Mateus[1]
[1] Instituto de Pesquisa e Desenvolvimento, Universidade do Vale do Paraíba, São José dos Campos, 12244-000, SP, Brazil; spilling@univap.br
[2] Departamento de Física, Universidade Tecnológica Federal do Paraná, Medianeira, 85884-000 PR, Brazil
[3] Departamento de química, Universidade Federal de Minas Gerais—UFMG, Belo Horizonte, 31270-901, MG, Brazil
[4] Departamento de Química, Centro Federal de Educação Tecnológica de Minas Gerais, Belo Horizonte, MG 5253, Brazil

Received 2022 November 23; revised 2023 May 30; accepted 2023 May 31; published 2023 July 14

Abstract

Within the cold regions of space, ices that are enriched with carbon monoxide (CO) molecules are exposed to ionizing radiation, which triggers new reactions and desorption processes. Laboratory studies on astrochemical ices employing different projectiles have revealed the appearance of several new species. In this study, we employed the upgraded PROCODA code, which involves a calculation phase utilizing thermochemistry data, to map the chemical evolution of pure CO ice irradiated by cosmic-ray analogs. In the model, we have considered 18 different chemical species (six observed: CO, CO_2, C_3, O_3, C_2O, and C_5O_3; 12 unobserved: C, O, C_2, O_2, CO_3, C_3O, C_4O, C_5O, C_2O_2, C_2O_3, C_3O_2, and C_4O_2) coupled at 156 reaction routes. Our best-fit model provides effective reaction rates (effective rate constants, (ERCs)), branching ratios for reactions within reaction groups, several desorption parameters, and the characterization of molecular abundances at the chemical equilibrium (CE) phase. The most abundant species within the ice at the CE phase were atomic oxygen (68.2%) and atomic carbon (18.2%), followed by CO (11.8%) and CO_2 (1.6%). The averaged modeled desorption yield and rate were 1.3e5 molecules ion^{-1} and 7.4e13 molecules s^{-1}, respectively, while the average value of ERCs in the radiation-induced dissociation reactions was 2.4e-1 s^{-1} and for the bimolecular reactions it was 4.4e-24 cm^3 molecule^{-1} s^{-1}. We believe that the current kinetics study can be used in future astrochemical models to better understand the chemical evolution of embedded species within astrophysical ices under the presence of an ionizing radiation field.

Unified Astronomy Thesaurus concepts: Astrochemistry (75); Laboratory astrophysics (2004)

1. Introduction

Carbon monoxide (CO) is one of the most abundant molecules throughout the universe, and, according to Huang et al. (2020), serves as the dominant carbon reservoir in molecular gas. CO is not only ubiquitous in the gas phase of several regions of the interstellar medium (ISM; e.g., Lacy et al. 1984; Ehrenfreund & Cami 2010, and references therein), but its detection in astrophysical ices in cold interstellar and circumstellar regions has also become routine (e.g., Herbst & van Dishoeck 2009; Boogert et al. 2015, and references therein). Furthermore, frozen CO has been found on the surface of the moon and planetary surfaces, such as those of Triton (Lellouch et al. 2010) and Pluto (Bertrand & Forget 2016), and is believed to exist in cold exoplanets as well (e.g., Beaulieu et al. 2006).

The ionizing radiation that primarily triggers chemical reactions within astrophysical ices comprises cosmic rays, UV, and soft X-rays, and fast electrons. Studies have suggested that the bombardment of frozen species, including CO, by incoming radiation from the ISM can augment the molecular complexity of these regions (e.g., de Araujo Vasconcelos et al. 2017; Boduch et al. 2015; Pilling et al. 2011, 2010a, Pilling et al. 2009; Palumbo et al. 2008; Andrade et al. 2008, and references therein).

Over the last 20 yr, several groups have performed laboratory experiments to evaluate the chemical changes induced by ionizing radiation in CO ices at cryogenic temperatures (e.g., Huang et al. 2020; Dartois et al. 2021; Ciaravella et al. 2016, 2012; de Barros et al. 2011; Seperuelo Duarte et al. 2010; Bennett et al. 2009; Palumbo et al. 2008; Jamieson et al. 2006; Loeffler et al. 2005; Trottier & Brooks 2004; Cottin et al. 2003; Gerakines et al. 1996; Cecchi-Pestellini & Aiello 1992). According to Jamieson et al. (2006), the main products of frozen CO irradiation can be sorted into three groups: carbon chains C_n, suboxides, C_nO, and C_nO_2 species (we also add here a fourth group containing the O_n). As discussed by Seperuelo Duarte et al. (2010) and Palumbo et al. (2008) and references therein, the major product from the processing of CO ice is carbon dioxide (CO_2). This species has also been detected extensively in the ISM in both gas and solid phase (e.g., Whittet et al. 1998; Gibb et al. 2004, and references therein). A recent review on the detection of CO and CO ices in the outer solar system is presented by Ahrens et al. (2022). The diatomic carbon (C_2) was detected by Souza & Lutz (1977) in the ISM toward the star Cyg OB2 with low excitation temperatures (30–40 K) suggesting some ice chemistry rule. This species has also been observed in comets (Lin et al. 2020 and references therein). The other produced species, such as the triatomic carbon (C_3), dicarbon monoxide (C_2O), and tricarbon monoxide (C_3O) have been often observed in molecular clouds (e.g., Ohishi et al. 1991; Cernicharo et al. 2000; Mookerjea et al. 2010; Urso et al. 2019). A discussion raised in the literature pointed out that the ratio C_2O/C_3O observed toward protostars should be ruled by some processing in the ice phase since gas-phase models fail to explain the observations (e.g., Urso et al. 2019). Moreover, Cernicharo et al. (2021) noticed that species such as C_3O and C_5O in molecular clouds (e.g., TMC-1) seem to have abundances larger than other C_nO oxides with n even (such as C_4O), but the understanding of this issue has yet to come. Palumbo et al. (2008) have suggested that the observation of carbon suboxide (C_3O_2), another product from the processing of CO ice by radiation, is also expected to be presented in the ISM due to the desorption of radiolysis products of grains to the gas phase. Tentative detection of this species in comet Halley has been reported (Huntress et al. 1991; Crovisier et al. 1991).

The goal of this study is to assess and quantify the presence of chemical species (and its reaction routes including its molecular kinetics) observed and predicted in pure CO ice subjected to bombardment by cosmic-ray analogs, using the PROCODA code (Pilling et al. 2022, 2023; Carvalho et al. 2022) and experimental data from Seperuelo Duarte et al. (2010). The experimental data involved the irradiation of pure CO ice at 13 K by 50 MeV Ni ions, obtained at the GANIL laboratory in France. A total of 156 coupled chemical reactions containing 18 chemical species within the ice were examined, with six observed species in the experimental study, including CO, CO_2, C_3, O_3, C_2O, and C_5O_3, and 12 unobserved species, including C, O, C_2, O_2, CO_3, C_3O, C_4O, C_5O, C_2O_2, C_2O_3, C_3O_2, and C_4O_2.

Briefly, the PROCODA code solves a system of chemically coupled differential equations applied for astrochemistry research (details in Pilling et al. 2022). It describes the evolution of the molecular concentration of astrophysical ice analogs under processing by radiation providing important information about the molecular kinetics of the system. The code calculates the effective rate constants (ERCs) of the direct radiation-induced reactions and bimolecular reactions. It is worth noting that the direct reactions handled here also consider the dissociation or destruction reactions triggered by the incoming radiation (which might also involve the action of fast secondary electrons within the ice). Additionally, the code calculates the radiation-induced desorption rate constants, the evolution of the desorption column density for the studied species as a function of time, and the summed molecular desorption yield (and desorption rate). Finally, the code provides abundances for both observed and unobserved (also referred to as unknown) species in the infrared (IR) spectra during the ice chemical evolution during processing by incoming radiation, and it also characterizes the chemical equilibrium (CE) phase in the ice that occurs at larger radiation fluence.

The current code version employs the ERCs ordering hypothesis based on thermochemistry data (taken from the literature), which incorporates actual chemical information into the code, specifying that some reactions should be faster than others. As discussed by Pilling et al. (2023), this procedure reduces code degeneracy and yields a more accurate chemical solution.

It is worth noting that the current methodology emphasizes the use of the term ERC, which has a broader concept than the *ordinary* rate constant of a reaction, commonly considered in gas-phase chemistry. The ERC defines the relationship between the column density of reactants and the rate of the chemical reaction. Unlike the gas phase, where reactants are surrounded by identical neighbors, the ERC accounts for the fact that reactants in the ice are surrounded by different neighbors that vary with time and are affected by the local density and temperature of the grain due to incoming radiation. Therefore, the ERC represents an average value in time and space over the ice during radiation processing and better describes what is happening within the ice in real conditions.

To provide more realistic results, the astrochemical ice models should consider this ERC instead of an ordinary rate constant for a given reaction (often employed the gas-phase values also for ices) since the ice composition is not strictly homogeneous and also varies with time, and also under radiation processing.

The computational methodology and details of the experimental data used are described in Section 2, while Section 3 presents the results, including the ERC calculations for the studied reactions, branching ratios within the reaction groups, desorption parameters obtained by the model, and molecular abundances at the CE phase. In Section 2.4, we discuss the astrophysical implications of our findings and the relevance of the use of the calculated ERCs in the astrochemical models. Finally, Section 5 presents our main conclusions and closing remarks.

2. Methodology

In this study, we utilize the updated PROCODA code (described in detail by Pilling et al. 2022, 2023) to investigate the chemical evolution of pure CO ice under irradiation by cosmic-ray analogs, to calculate the ERCs, and to characterize the CE phase that occurs at larger radiation fluences. The term ERC is employed once again to account for the various chemical environments in which a given reaction can take place within the ice. This upgraded version also considered thermochemistry data to minimize the solution's degeneracy as we will discuss further.

The employed chemical network considered a total of 156 coupled equations describing the chemical evolution of selected molecules in pure CO ices under the presence of different ionizing radiation types (including direct and bimolecular reactions). The reaction set also includes 18 radiation-induced molecular desorption to take into account the frozen species that go to the gas phase during the irradiation. The proposed reaction network involves 18 different chemical species within the ice (six observed species from experiments: CO, CO_2, C_3, O_3, C_2O, and C_5O_3; 12 unobserved species: C, O, C_2, O_2, CO_3, C_3O, C_4O, C_5O, C_2O_2, C_2O_3, C_3O_2, and C_4O_2).

2.1. Experimental Data Set

The experimental data set considered here was taken from Seperuelo Duarte et al. (2010) and describes the irradiation of pure CO ice at 13 K by 50 MeV $^{58}Ni^{13+}$ ions, obtained at the GANIL laboratory in France. The data consists of a set of 16 pairs of points containing the molecular concentration, in units of column density, of six observed species (CO, CO_2, C_3, O_3, C_2O, and C_5O_3) with their respective irradiation times. Briefly, the gaseous sample was condensed on a cold CsI substrate and irradiated by ions with a constant flux of 1e9 cm^{-2} s^{-1} until the final fluence of 1.1e13 cm^{-2}. The initial CO column density provided by the authors was 1.6e18 molecules cm^{-2} (thickness $\sim$ 0.9 μm). Infrared spectra (FTIR) were collected at different fluences and the column density of identified species was determined from the area of bands in the spectra. The authors determined a destruction cross section of 1e-13 cm^2 and a desorption yield of 7e4 molecules ion^{-1}.

To increase the accuracy of the model, for each observed species, it was considered 2800 not equally spaced interpolated data points ranging from 0–10,000 seconds (∼2.8 hr). It is important to note that no structure was added or omitted from the modeled data during the interpolation process. A discussion of the interpolation processes and a comparison with a model obtained employing low-resolution interpolation data (considering few interpolation data points) are given in Appendix A.

2.2. Brief Description of PROCODA

The code solves a system of coupled differential equations to describe the chemical evolution, as a function of time, of typical astrophysical ices during the processing by ionizing radiation (see also Carvalho et al. 2022 and Pilling et al. 2022). The code details, including the employed equations, the coupled equation minimization algorithm (L_BFGS-B algorithm), its explanatory flowchart, input/output parameters, and the convergence criteria, are fully explained in Pilling et al. (2022).

As discussed by Pilling et al. (2022), the typical equation in the chemically coupled system solved by PROCODA code has the following parameters:

$$\frac{dN_i}{dt} = \left[-\mathrm{DES}_i(t) \quad - \sum_{d1} k_{d1} N_i(t) - \sum_{d2} k_{d2} N_i(t) N_a(t)/L \right] + \left[\sum_{p1} k_{p1} N_a(t) + \sum_{p2} k_{p2} N_a(t) N_b(t)/L \right] [\text{molecules cm}^{-2}\ \text{s}^{-1}], \tag{1}$$

where N_i is the column density of the given species i, in units of molecules per square centimeter, dN_i/dt is its column density variation along the time t, k values are the ERCs for the different reactions, and L indicates the sample average thickness in units of centimeters. The values k_{d1} and k_{d2} indicate the destruction (consumption) processes and values k_{p1} and k_{p2} indicate the production processes of a given species i, indirect and bimolecular radiation-induced reactions. The rates k_{d1} and k_{p1} represent the direct dissociation reactions induced by radiation and in units per second and the rates k_{d2} and k_{p2} represent the bimolecular collision reactions induced by radiation, in units of cm^3 molecules^{-1} s^{-1}. In this equation the $\mathrm{DES}_i(t) = k_{\mathrm{des},i} \quad \Omega_i(t)\ N_i(t)$ is the differential column density desorption, i.e., the number of molecules (or atomic species) that desorbs from ice to gas phase per square centimeter and per second due to incoming radiation, which also depends on the intrinsic desorption rate ($k_{\mathrm{des},i}$), in units per second, the and the dimensionless surface coverage of the species i as a function of time ($\Omega_{\mathrm{i}}(t)$). The values N_a and N_b indicate the column densities of species a and b, in units of molecules per square centimeter, respectively, which participate in the reaction to produce or consume the respective i species. A list with the fully employed equations is presented in Appendix B.

To solve the coupled chemical equations set, comparing modeled species with experimental data, the code employs a minimization process of a function referred to as the score function (SF) that evaluates how close the system is to its minimum global solution (see the full discussion in Pilling et al. 2022, 2023). This function includes several terms and constraints such as the term for the χ^2 function for a direct comparison with experimental data, the term for mass similarity criterion (MSC) between model and experiments, the term for the similarity between experimental desorption and modeled desorption yield (Y), and the condition for the achievement of the CE phase in the ice at larger fluences (by employing the slope similarity criterion (SSC)). Those similarity criteria and constraints are employed in a minimization process of an SF that evaluates how close the system is to its minimum global solution.

The considered SF employed in the minimization algorithm during the search for the best solution for the coupled chemical systems is

$$\begin{aligned} \mathrm{SF} = {} & p1 \times \sum \frac{(\mathrm{oCO}_{\mathrm{data}} - \mathrm{oCO}_{\mathrm{data}})^2}{\mathrm{oCO}_{\mathrm{data}}} \\ & + p2 \times \sum \frac{(\mathrm{oCO2}_{\mathrm{data}} - \mathrm{oCO2}_{\mathrm{model}})^2}{\mathrm{oCO2}_{\mathrm{data}}} + \\ & + p3 \times \sum \frac{(\mathrm{oC3}_{\mathrm{data}} - \mathrm{oC3}_{\mathrm{model}})^2}{\mathrm{oC3}_{\mathrm{data}}} \\ & + p4 \times \sum \frac{(\mathrm{oO3}_{\mathrm{data}} - \mathrm{oO3}_{\mathrm{model}})^2}{\mathrm{oO3}_{\mathrm{data}}} + \\ & + p5 \times \sum \frac{(\mathrm{oC2O}_{\mathrm{data}} - \mathrm{oC2O}_{\mathrm{model}})^2}{\mathrm{oC2O}_{\mathrm{data}}} \\ & + p6 \times \sum \frac{(\mathrm{oC5O3}_{\mathrm{data}} - \mathrm{oC5O3}_{\mathrm{model}})^2}{\mathrm{oC5O3}_{\mathrm{data}}} + \\ & + p7 \times [(1 - \mathrm{MSC}_f) + (1 - \mathrm{MSC}o_f) + (1 - \mathrm{MSC}o_m)] \\ & + p8 \times (1 - \mathrm{DSC}) + p9 \times (1 - \mathrm{SSC}), \end{aligned} \tag{2}$$

where the dimensionless parameters *p1–p9* in this equation are the weights of each term, used as a tool to search for the best solution during the computational minimization processes. In this equation, the $o[]_{\mathrm{data}}$ and $o[]_{\mathrm{model}}$ are the column density values of given observed species taken from the experimental interpolated data and their respective values calculated by the model. The parameter MSC_f is the model MSC (or model mass conservation), calculated considering the similarity between the initial column mass of the modeled system and the total column mass of the model at the final modeling time (at the largest time) (including both masses, at the ice and desorbed), $\mathrm{MSC}o_f$ and $\mathrm{MSC}o_m$ are the columns' MSC between the experimentally observed column mass and the observed column mass in the model at the final modeling time and at the middle of the modeling time, respectively. From these three parameters, we calculate a parameter called $\mathrm{MSC} = (\mathrm{MSC}_f \times 100\% + \mathrm{MSC}o_f \times 100\% + \mathrm{MSC}o_m \times 100\%)/3$, which also helps to indicate how good the solution of the system is compared with the observed data. The parameter DSC is the desorption similarity criterion, calculated considering the similarity of the input expected desorption yield (based on manuscripts with the experimental data employed) and the total molecular desorption yield computed by the model. The parameter SSC is the slope similarity criterion, which is related to the achievement of the CE phase in the ice at larger radiation fluence, as described in Pilling et al. (2022).

It is worth noting that the χ^2 function (also referred to as the summed CHI2) can be obtained directly from Equation (2) making $p1 = p2 = p3 = p4 = p5 = p6 = 1$ and $p7 = p8 = p9 = 0$. The χ^2 function is a parameter obtained considering the experimental column density data of the observed molecules (CO, CO_2, C_3, O_3, C_2O, and C_5O_3) and their modeled column density.

As described by Pilling et al. (2022), during a typical run the code performed several calculation loops until the best-fit solution was found (the one with the lowest summed chi-square function, represented by the symbol χ^2). During this iterative process, the ERCs obtained from the previous best-fit calculation are included as inputs for the subsequent calculations. This approach ensures that the ordering hypothesis is continually refined and improved with each iteration.

In the current computational methodology, we considered two different calculations phases: in phase 1, the calculations were performed considering the ordering hypothesis for the ERC, which takes into account the thermochemistry data of the chemical species, until the best solution (precursor best-fit model) is obtained (this happens when no further improvements in the solutions occur after recursive runs; typically 10–20 times); in phase 2, we remove the ordering hypothesis (and keeping all other fine-tune parameters unchanged) and start again the calculation considering, as the initial guess, the ERC's values obtained in phase 1 until the best-fit model is obtained. (The phase 2 calculation does not consider the exploratory stage anymore in the code, only having a large refinement stage in the code; details of these stages are given in Pilling et al. 2022.) This procedure, dispute of reducing the solution's degeneracy and guarantees the most accurate solution possible with the PROCODA code, also minimize eventual undesired bias due to the thermochemistry ordering hypothesis. The differences between the solutions obtained for phases 1 and 2 (the final best-fit model) are presented and discussed in Appendix C.

2.3. Ordering Hypothesis of the ERCs Based on Thermochemistry Data

In brief, the ERC ordering hypothesis based on thermochemistry data is a procedure designed to rank ERCs by reaction enthalpy, with exothermic reactions being prioritized due to their greater likelihood of occurring. This approach helps reduce solution degeneracy, thereby providing more accurate predictions of ERCs' abundances in astrophysical environments.

The current code version is divided into two phases for the calculations: phase 1 (calculations considering ERCs ordering hypothesis) and phase 2 (calculations not considering ERCs ordering hypothesis starting from phase 1 best solution). The ordering hypothesis considers two conditions set: the first ordering set (referred to as ordering within reaction groups, OG) considers, as a first approximation, that in a given set of reactions (same initial reactants) the reactions with smaller enthalpy variation, $\Delta_r H$ (more exothermic), are expected to have larger rate constants, k (faster reactions). The second ordering set (ordering within selected single reactions, OS) was applied for single reactions and considered that the 10% with the lowest reaction enthalpy (most exothermic) was faster than the 10% with the larger reaction enthalpy (most endothermic). This procedure helps avoid overestimating the ERCs of thermodynamically highly improbable reactions. It is worth noting that the single reactions are the direct and bimolecular reactions that do not belong to a given reaction group.

The thermochemical data used in the ordering hypothesis for the ERCs considers that all studied species are in the lowest energy level and formation enthalpies and reaction enthalpies are at the gas phase at the theoretical temperature of 0 K. Additional details of the ordering procedure are given at Pilling et al. (2023). A list of the chemical species and gas-phase formation enthalpies at 0 K ($\Delta_f H^0$) considered in this work is presented in Table 1. These species were chosen since they present the lowest formation enthalpy energies (a criterion employed in the enthalpy reaction calculation). The reaction enthalpies employed in the ordering hypothesis for the ERCs were calculated from these listed formation enthalpies as we discuss further.

The set of reactions (outlined in Table 2) besides single reactions also contains reactions within groups, totaling 38 reaction groups (each one containing different reaction pathways) in the code, denoted as G1–G38. Each group has its own ordering in the ERCs, which is independent of the ordering in other groups. Single reactions (those not belonging to a specific reaction group) were not ranked by thermochemistry data. The rate constant ordering was introduced in the code by adding boundary constraints in the calculation of each rate of reaction

Table 1
Chemical Species and Gas-phase Formation Enthalpies at 0 K ($\Delta_f H^0$) Considered in This Work

Species (Additional Information)	$\Delta_f H^0$ (kJ mol^{-1})	References and Notes
C (triplet)	711.4	[1]
O (triplet)	246.8	[1]
C_2 (ethynylene, singlet)	820.3	[1]
CO^* (carbon monoxide, singlet)	−113.8	[1]
O_2 (molecular oxygen, triplet)	0	[1]
C_3 (tricarbon)	814.8	[1]
C_2O (CCO, dicarbon monoxide, triplet)	377.1	[1]
$CO_{2,}$(carbon dioxide, singlet)	−393.1	[1]
O_3 (ozone)	144.4	[1]
C_3O (CCCO, tricarbon monoxide)	330.0	[1]
C_2O_2 (OCCO, ethenedione)	14.9	[1, 4, 7]
CO_3 (singlet)	−126.9	[2, 5]
C_4O (CCCCO, triplet)	573.0	[2]
C_3O_2 (OCCCO, carbon suboxide)	−102.0	[2, 7]
C_2O_3 (OCOCO, Oxalic anhydride)	−282.2	[3]
C_5O (CCCCCO,singlet)	587.5	[2]
C_4O_2 (OCCCCO,triplet)	153.8	[2, 7]
C_5O_2 (OCCCCCO, singlet)	152.0	[2, 6, 7]

Note. [1] Obtained from the Active Thermochemical Tables v1.122p at https://atct.anl.gov/ (see also Ruscic et al. 2004, 2005; Ruscic & Bross 2020), [2] Calculated employing ORCA code (b3lyp def2-tzvp opt freq; https://orcaforum.kofo.mpg.de/app.php/portal (see also Neese et al. 2020), [3] Obtained from Gambi et al. (2001), [4] Additional information in Lewars (2008), [5] Additional information in Bennett et al. (2004), [6] Additional information in Jamieson et al. (2006), [7] Additional information in Wang et al. (2002).

Table 2

Reactions Considered in the Mapping of the Chemical Evolution of Pure CO Ice Irradiated by Cosmic Rays and the Main Outcomes from the Best-fit model, Including the ERCs (*k*_values) and the Branching Ratio (*k*_BR%) of Reactions within the Considered Reaction Groups

Reactants*	Products	*k*_name	*k*_value	*k*_BR%	$\Delta_R H$	*k*_type
CO_2 + RAD	O + CO	k1	1.45e-03 s^{-1}	86.93	526.15	Group 26 (k1, k3)
O + CO	CO2	k2	7.40e-26 cm^3 $molecules^{-1}$ s^{-1}	53.62	−526.15	Group 30 (k2, k57)
CO_2 + RAD	C + O_2	k3	2.18e-04 s^{-1}	13.07	1104.5	Group 26 (k1, k3)
C + O_2	CO_2	k4	3.04e-25 cm^3 $molecules^{-1}$ s^{-1}	98.21	−1104.5	Group 5 (k4, k58)
CO_2 + CO_2	O_2 + C_2O_2	k5	1.31e-25 cm^3 $molecules^{-1}$ s^{-1}	26.31	801.12	Group 25 (k9, k7, k5)
O_2 + C_2O_2	CO_2 + CO_2	k6	1.75e-23 cm^3 $molecules^{-1}$ s^{-1}	100.0	−801.12	Single
CO_2 + CO_2	O + C_2O_3	k7	1.80e-25 cm^3 $molecules^{-1}$ s^{-1}	36.14	750.86	Group 25 (k9, k7, k5)
O + C_2O_3	CO_2 + CO_2	k8	1.02e-23 cm^3 $molecules^{-1}$ s^{-1}	100.0	−750.86	Single
CO_2 + CO_2	CO + CO_3	k9	1.87e-25 cm^3 $molecules^{-1}$ s^{-1}	37.55	545.49	Group 25 (k9, k7, k5)
CO + CO_3	CO_2 + CO_2	k10	1.03e-25 cm^3 $molecules^{-1}$ s^{-1}	100.0	−545.49	Single
O + CO_2	CO + O_2	k11	1.24e-25 cm^3 $molecules^{-1}$ s^{-1}	9.57	32.47	Group 31 (k15, k11, k13)
CO + O_2	O + CO_2	k12	3.08e-25 cm^3 $molecules^{-1}$ s^{-1}	85.34	−32.47	Group 23 (k12, k65, k63)
O + CO_2	C + O_3	k13	1.39e-27 cm^3 $molecules^{-1}$ s^{-1}	0.11	1002.05	Group 31 (k15, k11, k13)
C + O_3	O + CO_2	k14	7.67e-24 cm^3 $molecules^{-1}$ s^{-1}	51.86	−1002.05	Group 6 (k14, k64)
O + CO_2	CO_3	k15	1.17e-24 cm^3 $molecules^{-1}$ s^{-1}	90.32	19.34	Group 31 (k15, k11, k13)
CO_3 + RAD	O + CO_2	k16	2.44e-01 s^{-1}	98.20	−19.34	Group 27 (k16, k66)
O_2 + CO_2	CO + O_3	k17	2.88e-23 cm^3 $molecules^{-1}$ s^{-1}	68.25	423.7	Group 34 (k17, k19)
CO + O_3	O_2 + CO_2	k18	7.30e-26 cm^3 $molecules^{-1}$ s^{-1}	75.65	−423.7	Group 24 (k18, k67)
O_2 + CO_2	O + CO_3	k19	1.34e-23 cm^3 $molecules^{-1}$ s^{-1}	31.75	513.02	Group 34 (k17, k19)
O + CO_3	O_2 + CO_2	k20	1.25e-26 cm^3 $molecules^{-1}$ s^{-1}	83.78	−513.02	Group 32 (k20, k68)
C + CO_2	C_2 + O_2	k21	6.21e-27 cm^3 $molecules^{-1}$ s^{-1}	0.62	502.05	Group 4 (k23, k25, k21)
C_2 + O_2	C + CO_2	k22	3.93e-25 cm^3 $molecules^{-1}$ s^{-1}	0.75	−502.05	Group 9 (k50, k98, k22)
C + CO_2	CO + CO	k23	5.08e-25 cm3 $molecules^{-1}$ s^{-1}	50.99	−545.88	Group 4 (k23, k25, k21)
CO + CO	C + CO_2	k24	1.85e-28 cm^3 $molecules^{-1}$ s^{-1}	4.72	545.88	Group 21 (k47, k24, k51, k49)
C + CO_2	C_2O_2	k25	4.82e-25 cm^3 $molecules^{-1}$ s^{-1}	48.38	−303.38	Group 4 (k23, k25, k21)
C_2O_2 + RAD	C + CO_2	k26	2.28e-01 s^{-1}	21.71	303.38	Group 12 (k48, k26, k95, k97)
CO + CO_2	C_2O_3	k27	4.56e-26 cm^3 $molecules^{-1}$ s^{-1}	35.05	224.71	Group 22 (k27, k29, k31, k33)
C_2O_3 + RAD	CO + CO_2	k28	5.96e-01 s^{-1}	36.43	−224.71	Group 13 (k28, k75, k77, k99, k101)
CO + CO_2	O + C_2O_2	k29	3.72e-26 cm^3 $molecules^{-1}$ s^{-1}	28.59	768.65	Group 22 (k27, k29, k31, k33)
O + C_2O_2	CO + CO_2	k30	6.76e-24 cm^3 $molecules^{-1}$ s^{-1}	89.32	−768.65	Group 29 (k30, k76)
CO + CO_2	O_2 + C_2O	k31	2.43e-26 cm^3 $molecules^{-1}$ s^{-1}	18.68	884.03	Group 22 (k27, k29, k31, k33)
O_2 + C_2O	CO + CO_2	k32	4.92e-23 cm^3 $molecules^{-1}$ s^{-1}	53.83	−884.03	Group 33 (k32, k78)
CO + CO_2	C_2 + O_3	k33	2.30e-26 cm^3 $molecules^{-1}$ s^{-1}	17.68	1471.63	Group 22 (k27, k29, k31, k33)
C_2 + O_3	CO + CO_2	k34	4.15e-23 cm^3 $molecules^{-1}$ s^{-1}	88.45	−1471.63	Group 10 (k34, k102)
C_2O + CO_2	CO + C_2O_2	k35	7.26e-25 cm^3 $molecules^{-1}s^{-1}$	50.88	−82.91	Group 11 (k35, k37)
CO + C_2O_2	C_2O + CO_2	k36	4.11e-26 cm^3 $molecules^{-1}$ s^{-1}	100.0	82.91	Single
C_2O + CO_2	C + C_2O_3	k37	7.01e-25 cm^3 $molecules^{-1}$ s^{-1}	49.12	445.18	Group 11 (k35, k37)
C + C_2O_3	C_2O + CO_2	k38	3.34e-26 cm^3 $molecules^{-1}$ s^{-1}	100.0	−445.18	Single
C_2 + CO_2	CO + C_2O	k39	1.69e-24 cm^3 $molecules^{-1}$ s^{-1}	23.76	−163.9	Group 8 (k90, k39, k41)
CO + C_2O	C_2 + CO_2	k40	2.59e-24 cm^3 $molecules^{-1}$ s^{-1}	60.66	163.9	Group 20 (k40, k61)
C2 + CO_2	C + C_2O_2	k41	7.02e-25 cm^3 $molecules^{-1}$ s^{-1}	9.87	299.07	Group 8 (k90, k39, k41)
C + C_2O_2	C2 + CO_2	k42	1.20e-25 cm^3 $molecules^{-1}$ s^{-1}	12.61	−299.07	Group 2 (k88, k62, k42)
CO_2 + O_3	O_2 + CO_3	k43	6.79e-24 cm^3 $molecules^{-1}$ s^{-1}	100.0	121.79	Single
O_2 + CO_3	CO_2 + O_3	k44	6.28e-27 cm^3 $molecules^{-1}$ s^{-1}	100.0	−121.79	Single

Table 2

(Continued)

Reactants*	Products	*k*_name	*k*_value	*k*_BR%	$\Delta_R H$	*k*_type
CO + RAD	C + O	k45	$\leqslant$ 1.00e-08 s^{-1}	100.0	1072.03	Single
C + O	CO	k46	$\leqslant$ 5.87e-31 cm^3 molecules^{-1} s^{-1}	100.0	−1072.03	Single
CO + CO	C_2O_2	k47	2.57e-27 cm^3 molecules^{-1}s^{-1}	65.63	242.5	Group 21 (k47, k24, k51, k49)
C_2O_2 + RAD	CO + CO	k48	8.11e-01 s^{-1}	77.21	−242.5	Group 12 (k48, k26, k95, k97)
CO + CO	C_2 + O_2	k49	8.15e-28 cm^3 molecules^{-1} s^{-1}	20.81	1047.93	Group 21 (k47, k24, k51, k49)
C_2 + O_2	CO + CO	k50	3.63e-23 cm^3 molecules^{-1} s^{-1}	69.28	−1047.93	Group 9 (k50, k98, k22)
CO + CO	O + C_2O	k51	3.46e-28 cm^3 molecules^{-1} s^{-1}	8.84	851.56	Group 21 (k47, k24, k51, k49)
O + C_2O	CO + CO	k52	4.70e-23 cm^3 molecules^{-1} s^{-1}	61.60	−851.56	Group 28 (k52, k96)
C + CO	C_2O	k53	1.08e-26 cm^3 molecules^{-1} s^{-1}	99.99	−220.47	Group 3 (k53, k55)
C_2O + RAD	C + CO	k54	3.48e-02 s^{-1}	100.0	220.47	Single
C + CO	O + C_2	k55	$\leqslant$ 5.87e-31 cm^3 molecules^{-1} s^{-1}	0.01	469.58	Group 3 (k53, k55)
O + C_2	C + CO	k56	5.97e-26 cm^3 molecules^{-1} s^{-1}	100.0	−469.58	Single
O + CO	C + O_2	k57	6.40e-26 cm^3 molecules^{-1} s^{-1}	46.38	578.35	Group 30 (k2, k57)
C + O_2	O + CO	k58	5.54e-27 cm^3 molecules^{-1} s^{-1}	1.79	−578.35	Group 5 (k4, k58)
C_2 + CO	C + C_2O	k59	3.40e-26 cm^3 molecules^{-1} s^{-1}	17.89	381.98	Group 7 (k84, k59)
C + C_2O	C_2 + CO	k60	4.50e-26 cm^3 molecules^{-1} s^{-1}	38.69	−381.98	Group 1 (k82, k60)
CO +C_2O	C + C_2O_2	k61	1.68e-24 cm^3 molecules^{-1} s^{-1}	39.34	462.97	Group 20 (k40, k61)
C + C_2O_2	CO + C_2O	k62	3.06e-25 cm^3 molecules^{-1} s^{-1}	32.14	−462.97	Group 2 (k88, k62, k42)
CO + O_2	C + O_3	k63	1.35e-26 cm^3 molecules^{-1} s^{-1}	3.74	969.58	Group 23 (k12, k65, k63)
C + O_3	CO + O_2	k64	7.12e-24 cm^3 molecules^{-1} s^{-1}	48.14	−969.58	Group 6 (k14, k64)
CO + O_2	CO_3	k65	3.94e-26 cm^3 molecules^{-1} s^{-1}	10.92	−13.13	Group 23 (k12, k65, k63)
CO_3 + RAD	CO + O_2	k66	4.48e-03 s^{-1}	1.80	13.13	Group 27 (k16, k66)
CO + O_3	O + CO_3	k67	2.35e-26 cm^3 molecules^{-1} s^{-1}	24.35	89.32	Group 24 (k18, k67)
O + CO_3	CO + O_3	k68	2.42e-27 cm^3 molecules^{-1} s^{-1}	16.22	−89.32	Group 32 (k20, k68)
O_2 + RAD	O + O	k69	8.08e-01 s^{-1}	100.0	493.68	Single
O + O	O_2	k70	$\leqslant$ 5.87e-31 cm^3 molecules^{-1} s^{-1}	100.0	−493.68	Single
O_3 + RAD	O + O_2	k71	6.54e-03 s^{-1}	100.0	102.45	Single
O + O_2	O_3	k72	4.93e-27 cm^3 molecules^{-1} s^{-1}	100.0	−102.45	Single
C_2 + RAD	C + C	k73	2.31e-02 s^{-1}	100.0	602.45	Single
C + C	C_2	k74	$\leqslant$ 5.87e-31 cm^3 molecules^{-1}s^{-1}	100.0	−602.45	Single
C_2O_3 + RAD	O + C_2O_2	k75	7.54e-01 s^{-1}	46.09	543.94	Group 13 (k28, k75, k77, k99, k101)
O + C_2O_2	C_2O_3	k76	8.08e-25 cm^3 molecules^{-1} s^{-1}	10.68	−543.94	Group 29 (k30, k76)
C_2O_3 + RAD	O_2 + C_2O	k77	2.46e-01 s^{-1}	15.04	659.32	Group 13 (k28, k75, k77, k99, k101)
O_2 + C_2O	C_2O_3	k78	4.22e-23 cm^3 molecules^{-1} s^{-1}	46.17	−659.32	Group 33 (k32, k78)
C_3 + RAD	C + C_2	k79	3.27e-02 s^{-1}	100.0	717.07	Single
C + C_2	C_3	k80	$\leqslant$ 5.87e-31 cm^3 molecules^{-1} s^{-1}	100.0	−717.07	Single
C_3O + RAD	C + C_2O	k81	9.23e-04 s^{-1}	0.34	758.51	Group 14 (k83, k85, k81)
C + C_2O	C_3O	k82	7.13e-26 cm^3 molecules^{-1} s^{-1}	61.31	−758.51	Group 1 (k82, k60)
C_3O + RAD	C_2 + CO	k83	2.33e-01 s^{-1}	84.97	376.53	Group 14 (k83, k85, k81)
C_2 + CO	C_3O	k84	1.56e-25 cm^3 molecules^{-1} s^{-1}	82.11	−376.53	Group 7 (k84, k59)
C_3O + RAD	O + C_3	k85	4.03e-02 s^{-1}	14.70	731.49	Group 14 (k83, k85, k81)
O + C_3	C_3O	k86	2.32e-24 cm^3 molecules^{-1} s^{-1}	100.0	−731.49	Single
C_3O_2 + RAD	C + C_2O_2	k87	4.48e-01 s^{-1}	27.65	828.3	Group 15 (k89, k91, k87, k93)
C + C_2O_2	C_3O_2	k88	5.26e-25 cm^3 molecules^{-1} s^{-1}	55.25	−828.3	Group 2 (k88, k62, k42)
C_3O_2 + RAD	C_2 + CO_2	k89	7.64e-01 s^{-1}	47.16	529.23	Group 15 (k89, k91, k87, k93)

Table 2

(Continued)

Reactants*	Products	*k*_name	*k*_value	*k*_BR%	$\Delta_R H$	*k*_type
C_2 + CO_2	C_3O_2	k90	4.72e-24 cm^3 molecules^{-1} s^{-1}	66.37	−529.23	Group 8 (k90, k39, k41)
C_3O_2 + RAD	O + C_3O	k91	4.08e-01 s^{-1}	25.18	678.85	Group 15 (k89, k91, k87, k93)
O + C_3O	C_3O_2	k92	7.13e-24 cm^3 molecules^{-1} s^{-1}	100.0	−678.85	Single
C_3O_2 + RAD	O_2 + C_3	k93	1.17e-04 s^{-1}	0.01	916.66	Group 15 (k89, k91, k87, k93)
O_2 + C_3	C_3O_2	k94	1.66e-25 cm^3 molecules^{-1} s^{-1}	100.0	−916.66	Single
C_2O_2 + RAD	O + C_2O	k95	1.05e-02 s^{-1}	1.00	609.06	Group 12 (k48, k26, k95, k97)
O + C_2O	C_2O_2	k96	2.93e-23 cm^3 molecules^{-1} s^{-1}	38.40	−609.06	Group 28 (k52, k96)
C_2O_2 + RAD	C_2 + O_2	k97	8.59e-04 s^{-1}	0.08	805.43	Group 12 (k48, k26, k95, k97)
C_2 + O_2	C_2O_2	k98	1.57e-23 cm^3 molecules^{-1} s^{-1}	29.97	−805.43	Group 9 (k50, k98, k22)
C_2O_3 + RAD	C + CO_3	k99	3.93e-02 s^{-1}	2.40	866.66	Group 13 (k28, k75, k77, k99, k101)
C + CO_3	C_2O_3	k100	1.13e-26 cm^3 molecules^{-1} s^{-1}	100.0	−866.66	Single
C_2O_3 + RAD	C_2 + O_3	k101	6.02e-04 s^{-1}	0.04	1246.92	Group 13 (k28, k75, k77, k99, k101)
C_2 + O_3	C_2O_3	k102	5.42e-24 cm^3 molecules^{-1} s^{-1}	11.55	−1246.92	Group 10 (k34, k102)
C_4O + RAD	C + C_3O	k103	1.26e-01 s^{-1}	19.47	468.37	Group 16 (k107, k103, k105)
C + C_3O	C_4O	k104	1.72e-25 cm^3 molecules^{-1} s^{-1}	100.0	−468.37	Single
C_4O + RAD	C_2 + C_2O	k105	1.82e-02 s^{-1}	2.81	624.43	Group 16 (k107, k103, k105)
C_2 + C_2O	C_4O	k106	2.56e-26 cm^3 molecules^{-1} s^{-1}	100.0	−624.43	Single
C4O + RAD	CO + C_3	k107	5.03e-01 s^{-1}	77.72	127.83	Group 16 (k107, k103, k105)
CO + C_3	C_4O	k108	1.53e-25 cm^3 molecules^{-1} s^{-1}	100.0	−127.83	Single
C_4O_2 + RAD	C + C_3O_2	k109	1.22e-01 s^{-1}	11.45	455.59	Group 17 (k115, k113, k109, k117, k111)
C + C_3O_2	C_4O_2	k110	1.09e-26 cm^3 molecules^{-1} s^{-1}	100.0	−455.59	Single
C_4O_2 + RAD	C_2 + C_2O_2	k111	1.02e-03 s^{-1}	0.10	681.44	Group 17 (k115, k113, k109, k117, k111)
C_2 + C_2O_2	C_4O_2	k112	4.78e-26 cm^3 molecules^{-1} s^{-1}	100.0	−681.44	Single
C_4O_2 + RAD	C_3 + CO_2	k113	5.10e-01 s^{-1}	47.86	267.75	Group 17 (k115, k113, k109, k117, k111)
C_3 + CO_2	C_4O_2	k114	4.70e-25 cm^3 molecules^{-1} s^{-1}	100.0	−267.75	Single
C_4O_2 + RAD	CO + C_3O	k115	3.92e-01 s^{-1}	36.79	62.41	Group 17 (k115, k113, k109, k117, k111)
CO + C_3O	C_4O_2	k116	1.26e-25 cm^3 molecules^{-1} s^{-1}	100.00	−62.41	Single
C_4O_2 + RAD	O + C_4O	k117	4.05e-02 s^{-1}	3.80	666.07	Group 17 (k115, k113, k109, k117, k111)
O + C_4O	C_4O_2	k118	9.54e-27 cm^3 molecules^{-1} s^{-1}	100.0	−666.07	Single
C_5O + RAD	C + C_4O	k119	1.43e-03 s^{-1}	2.77	696.89	Group 18 (k121, k123, k119)
C + C_4O	C_5O	k120	9.01e-25 cm^3 molecules^{-1} s^{-1}	100.0	−696.89	Single
C_5O + RAD	C_2 + C_3O	k121	2.02e-02 s^{-1}	39.12	562.81	Group 18 (k121, k123, k119)
C_2 + C_3O	C_5O	k122	1.01e-23 cm^3 molecules^{-1} s^{-1}	100.0	−562.81	Single
C_5O + RAD	C_3 + C_2O	k123	3.00e-02 s^{-1}	58.11	604.25	Group 18 (k121, k123, k119)
C_3 + C_2O	C_5O	k124	3.66e-24 cm^3 molecules^{-1} s^{-1}	100.0	−604.25	Single
C_5O_2 + RAD	C + C_4O_2	k125	1.52e-04 s^{-1}	0.01	713.14	Group 19 (k133, k135, k129, k131, k127, k125)
C + C_4O_2	C_5O_2	k126	3.87e-26 cm^3 molecules^{-1}s^{-1}	100.0	−713.14	Single
C_5O_2 + RAD	O + C_5O	k127	4.33e-01 s^{-1}	14.53	682.32	Group 19 (k133, k135, k129, k131, k127, k125)
O + C_5O	C_5O_2	k128	1.85e-26 cm^3 molecules^{-1} s^{-1}	100.0	−682.32	Single
C_5O_2 + RAD	C_2 + C_3O_2	k129	4.46e-01 s^{-1}	14.97	566.28	Group 19 (k133, k135, k129, k131, k127, k125)
C_2 + C_3O_2	C_5O_2	k130	1.66e-26 cm^3 molecules^{-1} s^{-1}	100.0	−566.28	Single
C_5O_2 + RAD	C_3 + C_2O_2	k131	5.52e-01 s^{-1}	18.53	677.51	Group 19 (k133, k135, k129, k131, k127, k125)
C_3 + C_2O_2	C_5O_2	k132	5.21e-26 cm^3 molecules^{-1} s^{-1}	100.0	−677.51	Single
C_5O_2 + RAD	CO + C4O	k133	7.12e-01 s^{-1}	23.90	307.18	Group 19 (k133, k135, k129, k131, k127, k125)
CO + C_4O	C_5O_2	k134	6.33e-24 cm^3 molecules^{-1} s^{-1}	100.0	−307.18	Single

Table 2
(Continued)

Reactants*	Products	k_name	k_value	k_BR%	$\Delta_R H$	k_type
C_5O_2 + RAD	$C_2O + C_3O$	k135	8.36e-01 s^{-1}	28.06	555.08	Group 19 (k133, k135, k129, k131, k127, k125)
$C_2O + C_3O$	C_5O_2	k136	5.53e-27 cm^3 $molecules^{-1}$ s^{-1}	100.0	−555.08	Single
$O_2 + O_2$	$O + O_3$	k137	5.16e-27 cm^3 $molecules^{-1}$ s^{-1}	100.0	391.23	Single
$O + O_3$	$O_2 + O_2$	k138	1.98e-25 cm^3 $molecules^{-1}$ s^{-1}	100.0	−391.23	Single
C desorption	⋯	k139	1.87e-03 s^{-1}	100.0	NA	Intrinsic desorption
O desorption	⋯	k140	7.81e-05 s^{-1}	100.0	NA	Intrinsic desorption
C_2 desorption	⋯	k141	5.25e-05 s^{-1}	100.0	NA	Intrinsic desorption
CO desorption	⋯	k142	1.45e-05 s^{-1}	100.0	NA	Intrinsic desorption
O_2 desorption	⋯	k143	4.97e-04 s^{-1}	100.0	NA	Intrinsic desorption
C_3 desorption	⋯	k144	1.60e-04 s^{-1}	100.0	NA	Intrinsic desorption
C_2O desorption	⋯	k145	2.87e-04 s^{-1}	100.0	NA	Intrinsic desorption
CO_2 desorption	⋯	k146	7.29e-04 s^{-1}	100.0	NA	Intrinsic desorption
O_3 desorption	⋯	k147	2.37e-05 s^{-1}	100.0	NA	Intrinsic desorption
C_3O desorption	⋯	k148	5.60e-04 s^{-1}	100.0	NA	Intrinsic desorption
C_2O_2 desorption	⋯	k149	8.61e-04 s^{-1}	100.0	NA	Intrinsic desorption
CO_3 desorption	⋯	k150	7.73e-04 s^{-1}	100.0	NA	Intrinsic desorption
C_4O desorption	⋯	k151	8.49e-04 s^{-1}	100.0	NA	Intrinsic desorption
C_3O_2 desorption	⋯	k152	7.06e-05 s^{-1}	100.0	NA	Intrinsic desorption
C_2O_3 desorption	⋯	k153	1.92e-04 s^{-1}	100.0	NA	Intrinsic desorption
C_5O desorption	⋯	k154	1.08e-05 s^{-1}	100.0	NA	Intrinsic desorption
C_4O_2 desorption	⋯	k155	9.65e-04 s^{-1}	100.0	NA	Intrinsic desorption
C_5O_2 desorption	⋯	k156	1.20e-05 s^{-1}	100.0	NA	Intrinsic desorption

Note. Δ_RH indicates the calculated enthalpy of the reaction at the gas phase (at the temperature of 0 K and considering the lowest formation enthalpy for each species). k_typeb indicates whether the reaction is within a group or is an individual reaction (single). See details and explanations in the text. * rad = radiation; ** NA = not available.

inside a specific reaction group. Additional details are given by Pilling et al. (2023).

2.4. Limitations and Advantages of the Code

The order of any chemical reaction is a parameter strictly determined experimentally (not always related to the stoichiometry of the reactants) and must be a non-negative value (does not need to be an integer) or zero. For example, in a reaction order of zero, the concentration of the reactants does not affect the rate of reaction. You could remove or add reactants to the mixture but the rate will not change. In a first-order reaction (order equal 1) the rate of the reaction is proportional to the amount of reactant and so on, i.e., doubling the concentration of a reactant also doubles the rate (e.g., Chang 2005). In the current kinetic model, we considered as a hypothesis that the overall reaction orders are determined by the sum of the number of reactants in each reaction (considering the order for each reactant equal to 1). Additionally, all desorption reactions in this manuscript were considered to be first-order reactions.

Related methodologies, which also compute rate constants from experiments by solving a system of coupled chemical equations, have employed different hypotheses for the order of the reactions, for example, assuming a first-type order or pseudo-first order for all reactions (e.g., Jamieson et al. 2006; Bennett et al. 2009, 2010; Bossa et al. 2015). These different assumptions can have significant impacts on the accuracy and precision of the resulting rate constants, as well as the overall understanding of the underlying chemical mechanisms. The present study takes a more comprehensive approach by considering direct, bimolecular, and radiation-induced desorption reactions in a more comprehensive set of coupled equations, which results in a more accurate and reliable determination of reaction kinetics and rate constants.

As pointed out by Pilling et al. (2022, 2023), the employed methodology of the PROCODA code does not consider, in an explicit way, the ionic and excited species. However, such chemical states should belong to the reactions inventory within the ice. The ERCs calculated here, for example, in the direct reaction (A + RAD $\rightarrow B + C$), (where RAD = any type of radiation) in some way involves the different chemical states in which A, B, or C species appear in the ice (which includes neutral, ionic, excited, and radical). The major difficulty in considering these forms separately in the models is not in writing the coupled equations, but in the way to measure them in the experimental data at the IR. In future work, we will try to introduce a few ionic species, in an explicit way, in the models (considering as a hypothesis, a specific fraction of ions in the signal measure in a given IR band). Additionally, here we do not consider individual activation energies since such quantities in the solid phase are highly dependent on the chemical environment and local temperature and density (see also Alves et al. 2021; Pilling & Bonfim 2020). Due to the constant exposure to radiation, astrophysical ices are able to overcome the activation barriers of most reactions through the absorption of incoming energy, as well as the distribution of energy within the ice by fast secondary electrons produced by the incoming radiation.

In spite of the employed hypothesis for ordering the ERCs and the highlighted limitations of the code (e.g., the limited number of species and chemical reactions), we expect the current results can provide precious information on the kinetics and the abundances of chemical species' CO-rich astrophysical ices that undergo processing by ionizing radiation, as well as precious information on the radiation-induced-desorption processes. It is worth noting that the current methodology also increases the accuracy of the final solution since the summed χ^2 function of the two sets of solutions slightly decreases from 0.88 (phase 1) to 0.79 (phase 2; the best-fit model). An extensive discussion of the code advantages, uncertainties, and limitations, is provided in Pilling et al. (2022, 2023).

3. Results

3.1. Evolution of Molecular Abundances and Calculation of ERCs

Figure 1 illustrates the evolution of column density for the most accurate model (model #F5h_phase2) generated with the PROCODA code (utilizing the ordering hypothesis of rate constants based on thermochemistry data) on pure CO ices irradiated by 50 MeV Ni ions (data from Seperuelo Duarte et al. 2010). Panel (a) presents the modeled abundances for the observed species only, and panel (b) presents all modeled species. The dashed line represents the modeled summed column density for desorbed species. The calculated summed χ^2 function for the best-fit model considering the similarity between the column densities from the experimental data set of six observed species and the calculated column densities in the model was 0.79. The summed desorption yield (Y) obtained in the model was 1.34e+5 molecules ion^{-1} (further discussion in Section 3.3). The MSC and SSC of the best-fit model were 99.21% and 98.64, respectively (see details in Pilling et al. 2023). This figure also reveals a remarkable match between experimental data and the best-fit model for most species, with the exception of C_5O_2.

In the case of C_5O_2, the current model suggests much smaller abundances than the observed values. This can be explained by at least two issues: (i) a lack of an important reaction to describe the chemical evolution of this species, and (ii) an overestimation in the abundance of this species from the experimental work. From the chemical point of view, the production of C_5O_2 requires at least five molecules of CO. It is unlikely that its abundances are larger than the abundance of C_2O or O_3 as suggested by the experimental work of Seperuelo Duarte et al. (2010). It is worth noting that the considered IR band of this species (at 2060 cm^{-1}) in the experiment is blended with other IR bands, and this might also introduce an error in the determination of both the band area, as well as in the determination of its band strength (see also Jamieson et al. 2006). Additionally, Huang et al. (2020) observed that in the irradiation of pure CO ices at 11 K with fast electrons (1000 eV), the maximum abundance of the produced C_2O is roughly 2.2 times larger than the abundance of C_5O_2. Future experimental investigation might help to solve this issue on the abundance of C_5O_2 produced by cosmic-ray processing of CO ices.

Figure 2 shows the evolution of column mass (column density times the molecular mass) as a function of time. As discussed by Pilling et al. (2022), the column mass is a quantity that helps us evaluate the mass conservation as the system evolves during the irradiation (this quantity also allows the quantification of the mass that goes to the gas phase by the desorption processes). The two vertical segments close to time 10,000 s were considered in the calculation of the SSC parameter (within the hypothesis of the CE stage at larger fluences). A very good match between the observed column mass (crosses) with the modeled observed mass (solid black line) can be seen in this figure. Blue, yellow, and red dashed lines represent the summed column mass for the desorbed species, the summed column mass for the unobserved species, and the summed mass in the model, respectively.

Table 2 lists the main results obtained for the best-fit models employing the PROCODA code (with the ordering hypothesis for the rate constants employing thermochemistry data) on pure CO ices irradiated by 50 MeV Ni ions (data from Seperuelo Duarte et al. 2010). The listed values include the calculated ERCs (k_values) and the branching ratio (k_BR%) for the considered reaction groups. The $\Delta_R H$ is the calculated enthalpy of the reaction at the gas phase (at the temperature of 0 K and considering the lowest formation enthalpy for each species). The parameter k_type indicates if the reaction is within a group or is single or is for desorption. The error in rate constants was estimated to be below 20% as discussed in Pilling et al. (2022).

The reactions outlined in Table 2 describe direct dissociation radiation-induced reactions, bimolecular reactions within the ice, and some desorption reactions driven by incoming radiation. An interesting point to consider is that these bimolecular reactions induced by incoming radiation could be related to diffusion-controlled bimolecular reactions (e.g., Shoup et al. 1981; Rice 1985; Burschka 1997; Atkins 1998; Konkoli 2009) because the incoming radiation supplies energy to the embedded species and makes them able to diffuse through the ice. Further research can explore the relationship between these two parameters, as well as the association between ERCs of the bimolecular reactions and other properties such as reaction binding energies, molecular diffusion, and viscosity. Finally, we would like to explicitly state that in this manuscript we can consider the ERCs as total reaction rates that may include a multitude of processes, especially since ions and excitations are not present.

The reaction enthalpies at the gas phase and 0 K ($\Delta_R H$), also presented in Table 2, employed in the ordering hypothesis for the ERCs, were calculated by the difference between the sum of the formation enthalpies of products and the sum of formation enthalpies of reactants in each reaction (see values in Table 1). It is noteworthy that some reactions considered in the model are endothermic (in the gas phase), and might not be able to occur at low temperatures. However, because the suited ices are constantly being bombarded (with constant energy input by the incoming projectiles), such reactions have a possibility of occurring.

From Table 2, it can be highlighted that the direct destruction of the observed species CO_2 preferentially yields the products O + CO (BR = 86.9%; k1). For the unobserved species, the direct destruction of CO_3, C_3O, C_4O, C_5O, C_2O_2, C_2O_3, C_3O_2,

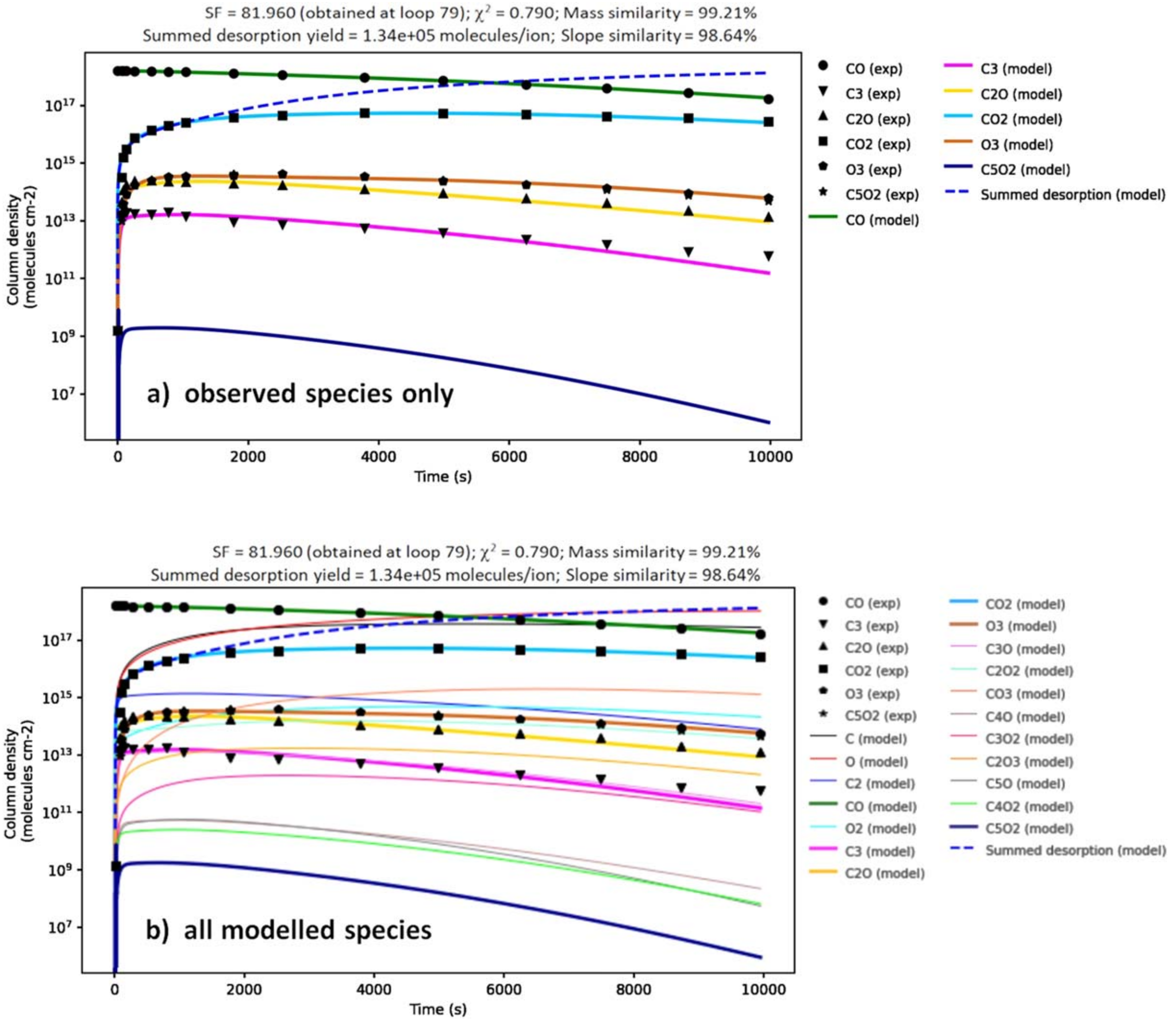

Figure 1. The evolution of column density obtained for the best-fit model employing the PROCODA code (with the ordering hypothesis for the rate constants employing thermochemistry data) on pure CO ices irradiated by 50 MeV Ni ions (data from Seperuelo Duarte et al. 2010). The black symbols represent the experimental data (observed species: CO, C_3, C_2O, CO_2, O_3, and C_5O_2). The data for O_3 and C_5O_2 are very close. Panel (a) presents models for the observed species only (for clarity purposes) and panel (b) displays all modeled species. The bold-dashed blue line represents the modeled summed desorption column density calculated in each model. Important output parameters for the best-fit models are displayed in the header. See the details in the text.

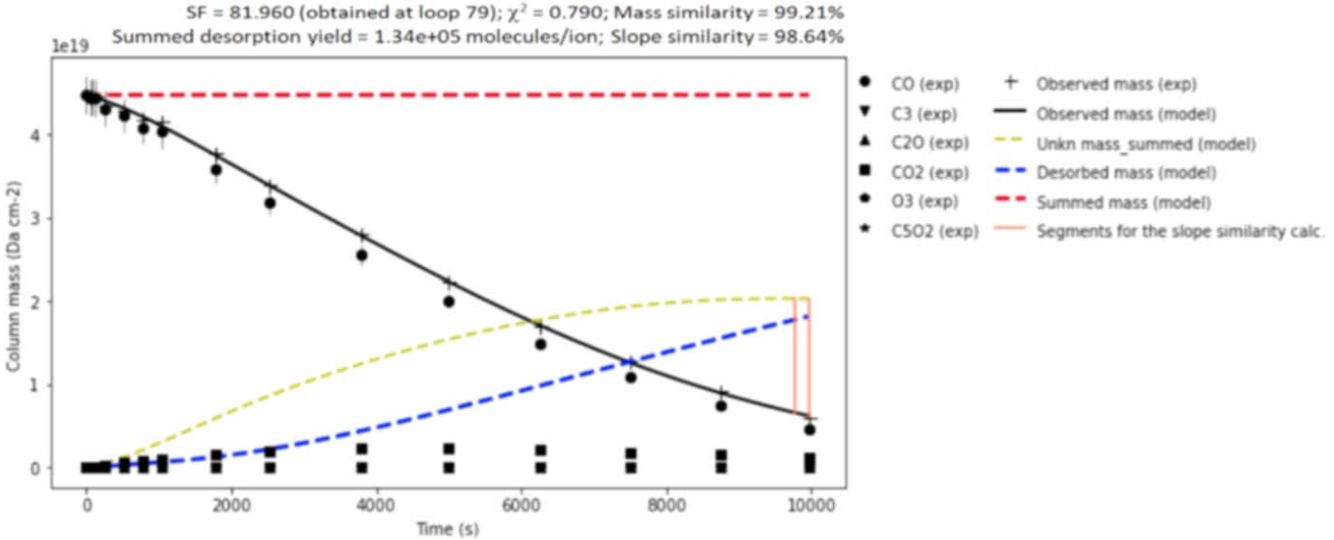

Figure 2. Evolution of column mass (column density × molecular mass) as a function of time of the best-fit model. The two vertical segments close to time 10,000 s were considered in the calculation of the SSC parameter (within the hypothesis of the CE stage at larger fluences). See the details in the text.

Table 3
Average Values for the ERCs and Desorption Parameters Obtained by the Best-fit Model Considered in the Mapping of the Chemical Evolution of Pure CO Ice Irradiated by Cosmic Rays

Average Parameter	Pure CO Ice at 13 K Irradiated by 50 MeV Ni ions (This Work)	Pure CO_2 Ice at 13 K Irradiated by 52 MeV Ni Ions (Pilling et al. 2023)
ERC for the intrinsic desorption reactions (k_{des})	4.4e-04 s^{-1}	2.9e-03 s^{-1}
ERC for radiation-induced direct reactions (k_A)	2.4e-01 s^{-1}	7.5e-03 s^{-1}
ERC for the bimolecular reactions (k_{A+B})	4.4e-24 cm^3 $molecules^{-1}$ s^{-1}	2.4e-25 cm^3 $molecules^{-1}$ s^{-1}
Desorption rate	7.4e+13 molecules s^{-1}	1.3e+14 molecules s^{-1}
Desorption yield (Y)	1.3e+05 molecules ion^{-1}	8.0e+04 molecules ion^{-1}

Note. A comparison with the average values obtained for pure CO_2 ices obtained by using similar methodology (Pilling et al. 2023) is also listed for comparison purposes.

and, C_4O_2, preferentially yields the products O + CO_2 (BR = 98.2%, k16), C_2 + CO (BR = 84.9%, k83), C_3 + CO (BR = 77.7%, k107), C_3 + C_2O (BR = 58.1%, k123), CO + CO (BR = 77.21%, k48), O + C_2O_2 (BR = 46.1%, k75), C_2 + CO_2 (BR = 47.2%, k89), and C_3 + CO_2 (BR = 47.8%, k113), respectively. For a selected set of bimolecular reactions involving CO, the results indicate that collision with CO itself, CO_2, and C_2O primarily yields the products C_2O_2 (BR = 65.6%, k47), C_2O_3 (BR = 35.1%, k27), and C_2 + CO_2 (BR = 60.7%, k40), respectively.

By comparing the calculations from phase 1, which employed the ordering hypothesis for the ERCs with thermochemistry data, to phase 2, which omitted the ordering hypothesis and used the best-fit model from phase 1 as the initial guess, we observed some variations in the ERC values (and also the position of the branching ratio within its groups) for a limited number of reactions. This suggests that for such reactions the employment of gas-phase thermochemistry data to order the respective ERCs does not yield the final best solutions (see also Appendix C).

The current model supports previous findings by Palumbo et al. (2008) and Sicilia et al. (2012) that carbon-chain oxides like C_2O, C_3O, and C_3O_2 readily form at low radiation doses but decrease in abundance at higher doses. It is worth noting that following Jamieson et al. (2006) and Trottier & Brooks (2004) in the irradiation of CO ices by cosmic rays other longer carbon oxides, including C_6O, C_7O, C_7O_2, C_8O, and C_9O and longer carbon chains, including C_n with $4 < n < 9$ might be produced with very low abundances. These species were not considered in the current manuscript.

Table 3 presents, for comparison purposes, the average values of the ERCs, the desorption rate, and the desorption yield, obtained by the best-fit model considered in this work. A comparison with average values obtained for pure CO_2 ices obtained by employing a similar methodology (Pilling et al. 2023) is also listed. In general, with the exception of the ERC for the intrinsic desorption reactions (k_{des}), the current average ERCs' ice was larger than the calculated previously for the CO_2 ice, which might be associated with larger mobility/diffusion of CO in the ice under irradiation, in comparison with CO_2. The average desorption rate and yield (Y) were also larger in this work than the calculated value for CO_2 ice. Future investigation might help better explain such differences.

A comparison between the selected ERCs obtained with the current methodology with some rate constants taken from literature, in both solid and gas phases, is provided in Tables 4 and 5, respectively. Table 4 presents a comparison of selected ERCs (direct reactions involving CO and CO_2) with some rate constants at the solid phase taken from literature, which describes a simple kinetic model to map the chemical evolution of CO_2 (Bennett et al. 2010) and CO ices (Bennett et al. 2009 Jamieson e al 2006), both irradiated by kiloelectronvolt electrons. Differently from the current work, which considers, direct, bimolecular, and radiation-induced desorption reactions, the described literature models employ a number of reactions and chemical species smaller than in the current work, and additionally, all reactions were considered to be of the first order (distributed in one, two, and three step mechanisms). The calculated ERC for the direct dissociation reaction of CO_2 to CO + O was only one order of magnitude lower than that calculated by Bennett et al. (2010). This table also presents some rate constants determined directly from the experimental papers employing cosmic-ray analogs (calculated from the experimental *effective* destruction cross section) taken from Pilling et al. (2010a, 2010b) and Seperuelo Duarte et al. (2009). Overall, the present study contributes to the growing body of research aimed at elucidating the mechanisms of CO and CO_2 dissociation under cosmic-ray bombardments and provides a basis for further exploration in this area.

In the current work, it is worth noting that the ERCs for direct reactions not only consider the excitation processes triggered by the incoming radiation but also take into account the collisions with secondary electrons within the ice, which can result in the given products (e.g., $A + \text{RAD} \rightarrow A^* \rightarrow \text{products}$). Such consideration for the excited species is also employed in the calculations of bimolecular reactions. More detailed descriptions of these excitation processes can be found in studies such as those of Jamieson et al. (2006) and Bennett et al. (2010).

Table 5 presents, for comparison purposes, the ERCs for selected reactions obtained with the current methodology with some rate constants at the gas phase taken from different works in the literature (e.g., Mallard et al. 2004; Gredel et al. 1989; van Dishoeck 1988; van Dishoeck et al. 2006; Husain & Young 1975; Heays et al. 2017). The ERCs values obtained for direct radiation-induced reactions in this study are much higher than the corresponding gas-phase values. This discrepancy is likely due to the fact that ERCs account for multiple processes,

Table 4
Comparison between Selected ERCs with Rate Constants at the Solid Phase from the Literature

Selected Reactions[a]	Solid-phase ERC in Pure CO_2 Ice Irradiated by CRs (This Work)	Solid-phase Rate Constant (Literature)	Notes and References (Literature)
$CO_2 + RAD \rightarrow O + CO$ $CO_2 + RAD \rightarrow C + O_2$	k1 = 1.45e-03 s^{-1} k3 = 2.18e-03 s^{-1}	…	Modeling experimental data employing 50 MeV Ni ions on pure CO ice [5]
$CO_2 + EL \rightarrow CO + O$	…	∼ 1.7e-5 s^{-1} [b]	From the irradiation of CO_2:$C^{18}O_2$ (1:2) at 10 K by 5 keV electrons [1]
$CO_2 + EL \rightarrow X$	…	∼ 4e-5 s^{-1} [b]	From the irradiation of CO_2:$C^{18}O_2$ (1:2) at 10 K by 5 keV electrons [1]
$CO_2 + RAD \rightarrow X$	…	3.6e-4 s^{-1} [c]	From the irradiation of CO_2 at 13 K by 52 MeV ions [3]
$CO_2 + RAD \rightarrow X$	…	3.4e-4 s^{-1} [c]	From the irradiation of CO_2 at 13 K by 46 MeV Ni ions [4]
$CO + RAD \rightarrow C + O$	k45 = <1e-08 s^{-1}	…	Modeling experimental data employing 50 MeV Ni ions on pure CO ice [5]
$CO + EL \rightarrow X$	…	2.9e-4 s^{-1} [d]	From the irradiation of CO ice at 15 K by keV electrons [2]
$CO + EL \rightarrow X$		∼4.2e-5 s^{-1} [e]	From the irradiation of ^{13}CO:$C^{18}O$ (1:1) at 10 K by 5 keV electrons [1], [6]
$CO + RAD \rightarrow X$	…	1e-4 s^{-1} [c]	From the irradiation of CO ice 13 K 50 MeV Ni ions [5]
$CO + RAD \rightarrow X$	…	3e-5 s^{-1} [c]	From the irradiation of CO ice at 13K 537 MeV Ni ions [5]

Notes.
[a] X indicates an unspecified product.
[b] Rates from the average destruction of CO_2 and $C^{18}O_2$. In this model all reactions were considered of first order (distributed in one, two, and three step mechanisms).
[c] k calculated from the multiplication of ion flux and dissociation cross section (determined from associative exponential function to the experimental data).
[d] Occurs in the presence of additional CO (excited) species typically yielding CO_2 and C. It was considered a pseudo-first-order reaction for the produced CO_2. The CO_2 is not destroyed or does not react once produced. Other reactions in the model are all of first order.
[e] Obtained from the average values of the destruction of ^{13}CO and $C^{18}O$. It was considered only first-order and pseudo-first-order reactions in the chemical network.
References. [1] Bennett et al. (2010), [2] Jamieson et al. (2006), [3] Pilling et al. (2010a), [4] Seperuelo Duarte et al. (2009), [5] Seperuelo Duarte et al. (2010), [6] Bennett et al. (2009).

including reactions with ionic and excited species, as well as collisions with secondary electrons within the ice. As a result, the reactions occur faster than in the gas phase. This phenomenon has been previously discussed by Pilling et al. (2011) as a comparison of dissociation cross sections of organic species under X-ray bombardment in ices and gases.

The calculated ERC values for bimolecular reactions are several orders of magnitude smaller than those in the gas phase, possibly due to the limited mobility and diffusion of reactants within the ice bulk. Although the small values suggest a smaller role for collision processes in ice chemistry, it should be noted that some newly produced molecular species, such as C_2O_2, can only be explained by considering these collisions within the ices.

3.2. Molecular Abundances at CE

The molecular abundances at CE in percentage (= equilibrium branching ratio, EBR(%)) and in units of molecules per square centimeter (= column density at the CE phase, N_{CE}) obtained by the best-fit model during the mapping of the chemical evolution of pure CO ice irradiated by cosmic rays are listed in Table 6. The most abundant species in the ice at the CE phase were atomic oxygen (18.2%) and carbon (68.2%), followed by CO (11.8%) and CO_2 (1.6%). The abundances of large species such as C_xO_2 ($x = 5,4,3$) were very low (<0.01%). The ozone and molecular oxygen abundances were around < 0.01% (6.1e+13 molecules cm^{-2}) and around 0.4% (2.2e+14 molecules cm^{-2}), respectively.

Table 6 also highlights the significance of the present study, as it reveals that the majority of species (86.5%) at the CE phase were not observed in the laboratory experiment conducted by Seperuelo Duarte et al. (2010). This underscores the importance of using computational models to complement experimental studies and gain a more comprehensive understanding of complex chemical systems.

Figure 3 presents the molecular abundances at CE in percentage (= equilibrium branching ratio EBR%) obtained by the best-fit model employing the PROCODA code. Blue and red in the bar plots indicate the observed and the unobserved species in the experiment, respectively. Panel (a) presents the results obtained in this work (pure CO ice irradiated by 50 MeV Ni ions). Panel (b), for comparison purposes, displays the results obtained employing a similar methodology on pure CO_2 ice irradiated by cosmic rays (52 MeV Ni ions) as reported by Pilling et al. (2023).

A comparison with the CO_2 model shows that among the unobserved species, the most abundant species in percentage was the oxygen atoms, followed by carbon atoms in both irradiated ices. However, the ordering of the four most abundant species at the chemical equilibrium in these two experiments was quite different O, C, CO_2, and CO (in the irradiation of pure CO ice) and CO_2, O, CO, O_3 (in the irradiation of CO_2). Indicating that besides CO and CO_2 ices shares some chemical similarities, their chemical reaction pathways and product yield in the presence of incoming radiation vary considerably. Curiously, besides the large percentage of oxygen atoms in the irradiated CO ice, the production of oxygen-rich species is not enhanced, for

Table 5
Comparisons between Selected ERCs in Ices with Rate Constants at the Gas Phase

Selected Reactions	Solid-phase ERC in Pure CO_2 Ice Irradiated by CRs (This Work)	Gas-phase Rate Constant* (Literature)	Notes and References (Literature)
$CO + RAD \rightarrow C + O$	k45 = <1e-08 s^{-1}	1.3e-17 s^{-1} 2.0e-10 s^{-1} 4.6e-15 s^{-1}	Cosmic rays [2], UV photons [3], UV induced by cosmic rays [6]
$CO_2 + RAD \rightarrow CO + O$	k1 = 1.45e-03 s^{-1}	1.3e-17 s^{-1} 8.9e-10 s^{-1} 6.0e-14 s^{-1}	Cosmic rays [2], UV photons [4], UV induced by cosmic rays [6]
$CO + O_2 \rightarrow O + CO_2$	k12 = 3.1e-25 cm^3 molecule^{-1} s^{-1}	5.9e-12 cm^3 molecule^{-1} s^{-1}	Theoretical [1]
$CO_2 + O \rightarrow O_2 + CO$	k15 = 1.2e-24 cm^3 molecule^{-1} s^{-1}	2.5e-11 cm^3 molecule^{-1} s^{-1}	Theoretical [1]
$CO_2 + C \rightarrow C_2O_2$	k25 = 4.8e-25 cm^3 molecule^{-1} s^{-1}	< 1e-14 cm^3 molecule^{-1} s^{-1}	Under UVC photolysis [5]
$C_2O + O \rightarrow CO + CO$	k64 = 4.7e-23 cm^3 molecule^{-1} s^{-1}	8.6e-11 cm^3 molecule^{-1} s^{-1}	Theoretical [1]

Note. *α term only, of the Arrhenius-type formulae (see McElroy et al. 2013) [1] UMIST database (Mallard et al. 2004), [2] UMIST database (Gredel et al. 1989), [3] UMIST database (van Dishoeck 1988) [4] UMIST database (van Dishoeck et al. 2006), [5] Husain & Young (1975), [6] Heays et al. (2017).

example, O_2 or O_3. The production of such species seems to be enhanced only in the case of irradiated CO_2 ices.

Finally, the abundance of CO_3 at CE in the current model was also very low (0.09% = 1.3e+15 molecules cm^{-2}), indicating that this species is virtually negligible in the irradiation of pure CO ices as also observed in other experimental works (e.g., Gerakines et al. 1996; Satorre et al. 2000; Trottier & Brooks 2004). It is worth noting that, the abundance of CO_3 at the CE phase in the experiment of CO_2 was almost half (0.05%) the value found in the current experiment.

The electron irradiation experiments on CO ices have consistently shown that CO_2 is the most predominant reaction product, based solely on the observed species in the IR spectra (excluding atomic and unobserved species). This conclusion is supported by studies such as those of Huang et al. (2020), Bennett et al. (2009), and Jameson et al. (2006). It is worth noting, however, that these studies were unable to measure the abundances of C and O atoms produced in the ice by the incoming radiation.

3.3. Molecular Desorption Induced by Cosmic Rays

The molecular desorption induced by cosmic rays obtained by the best-fit model during the mapping of the chemical evolution of pure CO ice irradiated by cosmic rays (50 MeV Ni ions) is illustrated in Figure 4. Panel (a) displays the desorption column density of the modeled species as a function of irradiation time. The arrows in the figure indicate regions in which the desorption of one species exceeds that of another, highlighting the complexity of the desorption processes over time. This behavior has been observed in previous models (Pilling et al. 2022, 2023) and underscores how the inventory and amount of molecules that go into the gas phase due to desorption change as the ice is irradiated, eventually reaching CE. Future astrochemical models must take these phenomena into account.

Table 6
Molecular Abundances at CE in Percentage (= Equilibrium Branching Ratio, EBR%) and in Units of Molecules per Square Centimeter (= Column Density at CE, N_{CE}) Obtained by the Best-fit Model During the Mapping of the Chemical Evolution of Pure CO Ice Irradiated by Cosmic Rays

Species	EBR (%)	N_{CE} (molecules cm^{-2})
C	18.2	2.8e+17
O	68.1	1.1e+18
C_2	0.05	8.3e+13
CO*	11.8	1.8e+17
O_2	0.4	2.2e+14
C_3	~ 0	1.5e+11
C_2O	<0.01	9.2e+12
CO_2	1.6	2.5e+16
O_3	<0.01	6.1e+13
C_3O	~0	2.2e+11
C_2O_2	<0.01	3.9e+13
CO_3	0.09	1.3e+15
C_4O	~0	2.5e+08
C_3O_2	~0	1.2e+11
C_2O_3	~0	2.2e+12
C_5O	~ 0	6.2e+07
C_4O_2	~ 0	7.4e+07
C_5O_2	~ 0	1.0e+07
Summed observed species	13.6	2.1e+17
Summed unobserved species	86.5	1.4e+18

Note. * Parent species (initial column density = 1.6e18 molecules per square centimeter).

The parent and abundant species CO is the dominant desorbed species throughout the entire experiment; however, the second most desorbed species (as well as the other desorption rank positions) depends on the irradiation time. For example, at the beginning of the experiment, C atoms were the second most important, but this changed with time being overpassed by the desorption of CO_2 and C_2. Panels (b) and (c) in Figure 4 present the intrinsic molecular desorption rate in units per second and the molecular desorption in percentage at the CE phase. Blue and red in the bar plots indicate the observed and the unobserved species in the experiment, respectively. C_2 presents the highest intrinsic desorption rate, followed by C_3, C, and CO_3. The desorption at the CE phase was dominated mainly by atomic carbon (77.5%) and oxygen (16.9%), followed by the parent species CO (~4.9%) and CO_2

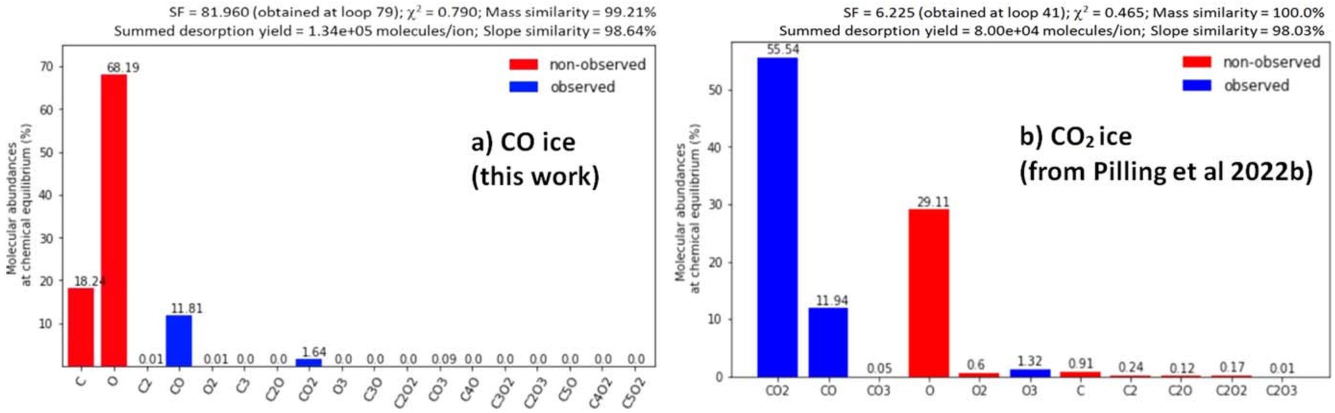

Figure 3. Molecular abundances at CE expressed as a percentage (= EBR%) obtained by the best-fit model. Blue and red in the bar plots indicate the observed and the unobserved species in the experiment, respectively. Pane a displays the results obtained in this work for pure CO ice irradiated by cosmic rays (50 MeV Ni ions). For comparison purposes, panel (b) shows the results obtained employing a similar methodology for pure CO_2 ice irradiated by cosmic rays (52 MeV Ni ions), taken from Pilling et al. (2023).

(∼0.6%). It is worth noting that the desorption yield and ice's molecular abundances at the equilibrium chemistry are different, expressed in percentage. For example, atomic oxygen dominates within the ice (68.2%), followed by atomic carbon (18.2%), CO (11.8%), and CO_2 (1.64%) at the equilibrium. This interesting result suggests that the dominant chemical pathways in gas-phase chemistry near irradiated icy grains may differ from those observed on the ice surface, leading to different chemistry.

The knowledge of desorption rates and the amount of molecular desorption induced by cosmic rays (determined at CE) are important for astrochemistry. These values can be used in astrochemical models to constrain the abundances of such species in the gas phase in very cold astrophysical environments. For example, the current work suggests that C_2 is the third most important desorbed species during the bombardment of pure CO ice by cosmic rays. The detection of such species from observations might indicate, for example, an intense and penetrating cosmic-ray field in molecular clouds or denser protostellar environments where astrophysical ices are richer in CO. Additionally, the measurement of the gas-phase CO/CO_2 ratio by radio observations might also be employed, combined with other measurements, as a diagnostic for cosmic rays processing CO-rich ices in astrophysical regions (the modeled desorbed CO/CO_2 ratio obtained in the CE phase in the current work was ∼9).

The results obtained here further validate the notion of cosmic-ray bombardment of CO ices being a key factor in the formation of long carbon chains in the ISM, as suggested by Trottier & Brooks (2004). This finding has implications for our understanding of the chemical composition and evolutionary history of the ISM.

4. Astrophysical Implications

The chemical evolution of ISM is a complex process that involves a large number of chemical reactions. To understand this process, it is necessary to have a good knowledge of the rate constants of these reactions. Since the presence of CO molecules in astrophysical ices are ubiquitous, being one of the most abundant species (e.g., Öberg et al. 2011; Boogert et al. 2015; Huang et al. 2020, and references therein), the understanding of reaction routes and the chemical kinetic of CO and CO-rich ices in space is, therefore, crucial in understanding the evolution of organic chemistry in the universe.

These models typically take into account the various physical and chemical processes that occur in the ISM, such as gas-phase reactions, grain surface chemistry, and photochemistry. By using these models, it is possible to investigate the chemical evolution of the ISM under different conditions, such as varying radiation fields, temperatures, and densities (e.g., Cuppen et al. 2017; Eistrup & Henning 2022; Rocha et al. 2023).

The results presented here, especially the determined ERCs for the solid-phase reactions, the molecular abundances at the CE phase, and the molecular desorption yields, provide valuable information that can be used in astrochemical models to gain insights into astronomical observations. An important outcome of the current work is providing information on the molecular column density of atomic species and unobserved species in the irradiated ices (e.g., C, O, O_2, C_2, and C_nO oxides). We hope these findings can help in the analysis of the high-resolution IR observations from JWST of CO-rich protostellar ices. Moreover, we also expect that the desorption yield quantified in the current work can help in putting constraints on the gas chemistry and in the submillimeter observations from the Atacama Large Millimeter/submillimeter Array of cold molecular clouds and protoplanetary disks.

The complexity of ices exposed to radiation in space, particularly in the protostellar ices, requires chemical modeling that combines radiative transfer and reaction rates in both gas and solid state. The results obtained here can provide valuable input for such modeling efforts. Other studies, such as those of Ballering et al. (2021) and Rocha et al. (2023), have emphasized the importance of such modeling in understanding the chemical evolution of ices in space. Therefore, the findings of this study are expected to contribute significantly to ongoing research efforts to deepen our understanding of the chemistry of the universe.

As highlighted by Jiménez-Escobar et al. (2016) and de Barros et al. (2022), the presence of CO molecules in ices that contain H-rich species or H atoms provides an environment for organic chemistry to evolve. Moreover, in addition to the importance of CO molecules in astrophysical ices, other molecules such as water (H_2O), methane (CH_4), and ammonia (NH_3) also play crucial roles in the formation and evolution of organic chemistry in space. These molecules are found in abundance in many astrophysical environments and are known to participate in numerous chemical reactions that lead to the formation of complex organic molecules. Furthermore, the study of ices in space has revealed the presence of complex

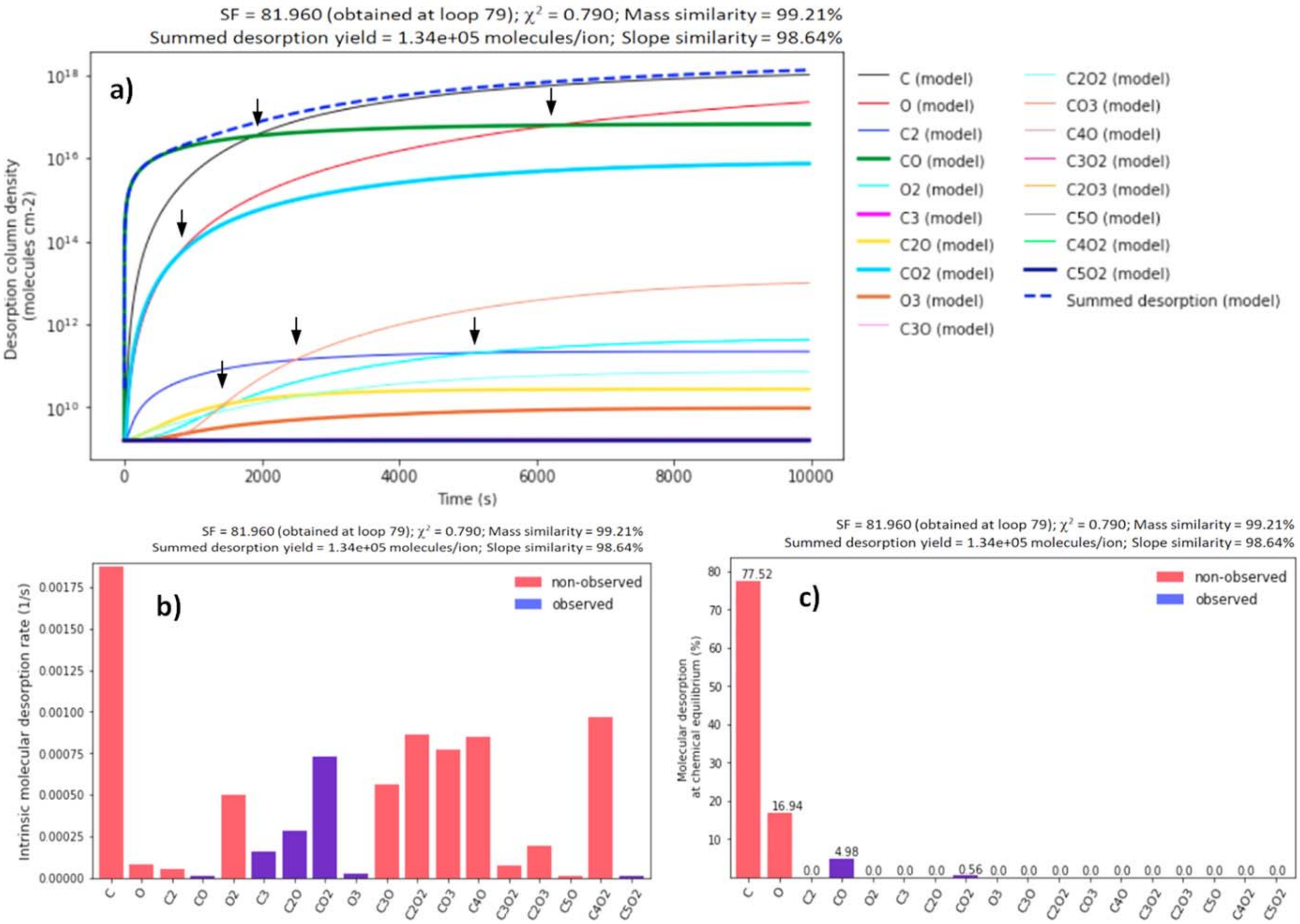

Figure 4. Molecular desorption induced by cosmic rays obtained by the best-fit model in the mapping of the chemical evolution of pure CO ice irradiated by cosmic rays (50 MeV Ni ions). Panel (a) shows the desorption column density of the modeled species as a function of irradiation time. Arrows indicate regions in which the desorption of certain species surpasses that of other species. Panels (b) and (c) display the intrinsic molecular desorption rate in units per second and the molecular desorption, in percentage, at the CE phase. Blue and red in the bar plots signify the observed and the unobserved species in the experiment, respectively. See the details in the text.

organic molecules, including amino acids, which are the building blocks of proteins. The study of astrophysical ices can, therefore, provide important clues to the fundamental questions of the origins of life and the possibility of life beyond Earth (Guélin & Cernicharo 2022).

In future research, the PROCODA code will be employed to provide a detailed understanding of the chemical evolution of ices containing CHONs atoms (e.g., mixed ices containing molecules with CHONs atoms) and accurately quantify the abundances of organic and prebiotic compounds when exposed to incoming ionizing radiation. This research could play an important role in helping to explain the presence of organic molecules in space, and could also provide insights into the formation of complex molecules in astrophysical ice analogs. Additionally, this research could be of great importance for astronomers, as it may shed light on the conditions that lead to the formation of prebiotic molecules in the universe.

It is also worth noting that the chemical processes that occur in astrophysical ices are not limited to the formation of organic molecules. These chemical processes, driven mainly by the incoming ionizing radiation, also play a critical role in shaping the physical properties of these ices, such as their structure, porosity, and optical properties (e.g., Bossa et al. 2014; Mainitz et al. 2016). In conclusion, the study of astrophysical ices, including the role of CO molecules, is a vital component in understanding the chemical evolution of ISM organic compounds but also provides valuable information for ongoing research efforts in astrochemistry and astrophysics.

5. Conclusions

In this manuscript, we present a theoretical model that uses the PROCODA code to map the chemical evolution and kinetics of pure CO ice irradiated by 50 MeV Ni ions. Here, we employed the upgraded version of the code, which adds an ordering hypothesis for the ERCs by employing thermochemistry data. The experimental data were taken from Seperuelo Duarte et al. (2010), which simulated the bombardment of CO ice at 13 K by cosmic-ray analogs. The main conclusions of this study are as follows.

The best-fit model ($\chi^2 = 0.79$) provides the ERCs for 156 reaction routes (including radiation-induced destruction reactions, bimolecular reactions, and desorption reactions) considering 18 species within the ice (six observed in laboratory experiments: CO, CO_2, C_3, O_3, C_2O, and C_5O_3; 12 unobserved: C, O, C_2, O_2, CO_3, C_3O, C_4O, C_5O, C_2O_2, C_2O_3, C_3O_2, and C_4O_2).

The branching ratio within the reaction groups was calculated indicating the preferential pathways. The radiation-induced direct destruction observed for CO_2 preferentially yields the products O + CO (BR = 86.9%; k1). For the unobserved species, the direct destruction of CO_3, C_3O, C_4O, C_5O, C_2O_2, C_2O_3, C_3O_2 and,

C_4O_2 preferentially yields the products O + CO_2 (BR = 98.2%, k16), C_2 + CO (BR = 84.9%, k83), C_3 + CO (BR = 77.7%, k107), C_3 + C_2O (BR = 58.1%, k123), CO + CO (BR = 77.21%, k48), O + C_2O_2 (BR = 46.1%, k75), C_2 + CO_2 (BR = 47.2%, k89), and C_3 + CO_2 (BR = 47.8%, k113), respectively. For bimolecular reactions, the preferential chemical pathways between the collision of CO with CO itself, CO_2 and C_2O, yield the product C_2O_2 (BR = 65.6%, k47), C_2O_3 (BR = 35.1%, k27), and the products C_2 + CO_2 (BR = 60.7%, k40), respectively.

The current model fails in the mapping of C_5O_2 data, yielding much lower abundances than observed in the experiment (Seperuelo Duarte et al. 2010). We suggest that this discrepancy could be due to a combination of factors, such as a restricted number of reactions considered in the model, and/or an imprecise determination of the abundance of C_5O_2 in the experimental data.

The most abundant species in the ice at the chemical equilibrium were atomic oxygen (18.2%) and carbon (68.2%), followed by CO (11.8%) and CO_2 (1.6%). The abundances of large species such as C_xO_2 (x = 5, 4, and 3) were very low (<0.01%). The ozone and molecular oxygen abundances were around <0.01% (6.1e+13 molecules cm^{-2}) and around 0.4% (2.2e+14 molecules cm^{-2}), respectively.

The molecular desorption at the CE phase was dominated mainly by atomic carbon and oxygen, followed by the parent species CO (~4.9%) and CO_2 (~0.6%). Since the abundance of desorbed gaseous species is different from the ice's abundance at the ice at the CE phase, this suggests that dominant chemical pathways in gas-phase chemistry near irradiated icy grains may differ from those observed on the ice surface, leading to different chemistry.

The results of this study provide valuable insights into the chemical evolution of CO-rich ices under radiation, which is a crucial aspect of solid-state astrochemistry. The study sheds light on the production of large carbon-chain molecules in the ISM, where the chemistry is dominated by reactions occurring on dust grains coated with ices. These molecules are of particular interest to astronomers as they are important precursors to complex organic molecules that are potential building blocks of life. By elucidating the reaction pathways and rates of CO-rich ices under irradiation, this study helps to refine and improve solid-state astrochemistry models, which can aid in the interpretation of astronomical observations.

Moreover, this study also has implications for the observation of frozen and desorbed molecules in cold space environments. These observations provide valuable information about the chemical composition of the ISM and the physical conditions in which the molecules are formed and evolve. The results of this study may help explain some of the observed molecular species and their abundances, as well as the mechanisms behind their formation and desorption. Therefore, this study has significant implications for our understanding of the chemistry and physics of the ISM, and the role they play in the formation of complex organic molecules and potentially life-supporting environments.

Acknowledgments

The authors acknowledge the Brazilian research agencies Conselho Nacional de Desenvolvimento Científico e Tecnológico—CNPq (#306145/2015-4; 302985/2018-2) and Coordenação de Aperfeiçoamento de Pessoal de Nível Superior—CAPES (#PNPD/88887.368365/2019-00; #PNPD/88887.751149/2022-00).

Data Availability

The data underlying this article will be shared on reasonable request to the corresponding author.

Appendix A
Additional Information on the Interpolation Process of the Input Data and Its Implication on the Calculation Minimization Procedure of the PROCODA Code

Figure A1 presents the original experimental data (black symbols), taken from Seperuelo Duarte et al. (2010), overlaid with its interpolated points (red points) employed to increase the accuracy of the model. It was considered, for each observed species, 2800 not equally spaced interpolated data points ranging from 0–10,000 seconds (~2.8 hr). It is important to note that no structure was added or omitted from the modeled data during the interpolation process. The employment of interpolation data (or high-resolution data) helps the employed minimization algorithm of the SF to find the best possible solution.

Figure A2 illustrates the employment of low-resolution interpolated data points (not equally spaced) in the procedure of solving a coupled equations set, to map the chemical evolution of pure CO ice irradiated by cosmic rays, using the PROCODA

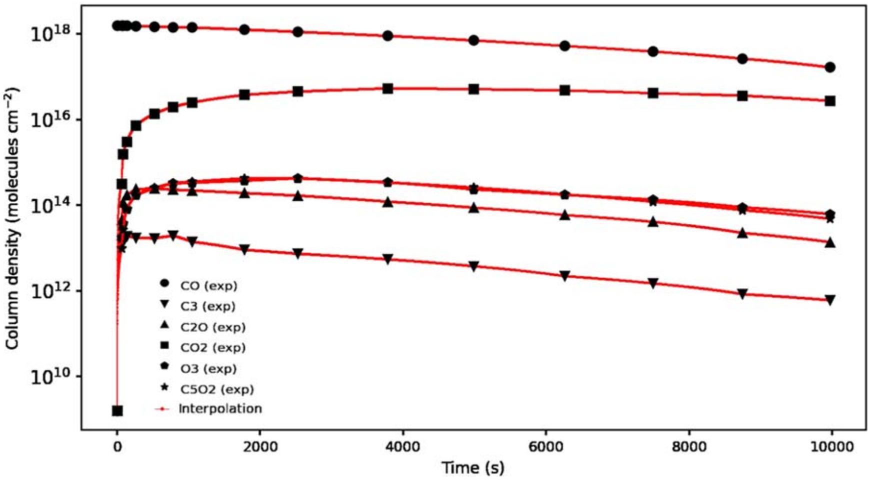

Figure A1. Comparison between experimental data (black symbols), taken from Seperuelo Duarte et al. (2010), and the interpolated experimental data (red points) employed in the models. As observed, the interpolation process did not add or miss any structure on the modeled data.

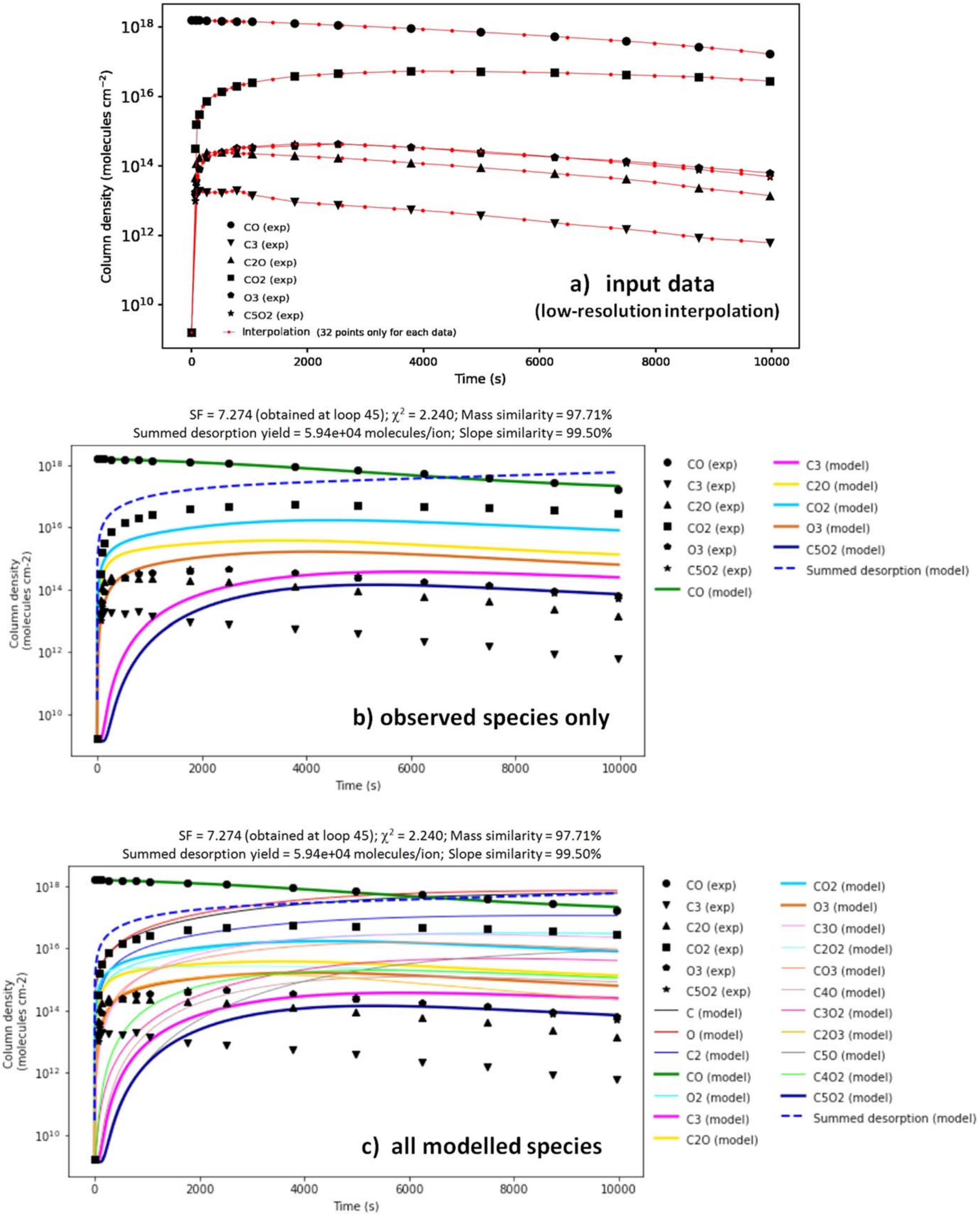

Figure A2. Results employing low-resolution interpolated data points in the PROCODA code for pure CO ice irradiated by cosmic rays. Panel (a) displays the experimental data (black symbols), taken from Seperuelo Duarte et al. (2010), overlaid with the low-resolution interpolated experimental data (red points) considering only 32 points per molecule for this analysis. Panels (b) and (c) present the best-fit solution obtained in this case, for the observed species only and for all modeled species, respectively. We observe that the use of low-resolution data points directly into the code does not guarantee obtaining the best solution with the employed minimization algorithm. See the details in the text.

code. Panel (a) displays a comparison between the experimental data (black symbols), taken from Seperuelo Duarte et al. (2010), and low-resolution interpolated experimental data (red points) considering only 32 points per molecule for this analysis. Panels (b) and (c) present the best-fit solution obtained in this case, for the observed species only and for all species, respectively (for comparison, see also Figure 1).

From Figure A2 we clearly notice that the use of low-resolution data points, directly into the code, does not guarantee obtaining the best solution with the employed minimization algorithm. For example, in this case, the code has difficulty fitting the beginning of irradiation time and several molecules with low values of column densities. This figure reinforces the utilization of a large input data set in the code.

Appendix B
Details on the Employed Coupled Equation System

The equations presented below describe the coupled equations system employed in the current PROCODA code for mapping the evolution of CO ice irradiated by cosmic rays. We considered 18 different chemical species within the ice (six observed: CO, CO_2, C_3, O_3, C_2O, and C_5O_3; 12 unobserved: C, O, C_2, O_2, CO_3, C_3O, C_4O, C_5O, C_2O_2, C_2O_3, C_3O_2, and C_4O_2), 156 reaction routes, including direct radiation-induced reactions and bimolecular collision reactions and radiation-induced desorption reactions.

$d[C]/dt = (-r139 - r4 - r14 - r21 - r23 - r25 - r38 - r42 - r46 - r53 - r55 - r58 - r60 - r62 - r64 - 2^{*}r74 - r80 - r82 - r88 - r100 - r104 - r110 - r120 - r126 + r3 + r13 + r22 + r24 + r26 + r37 + r41 + r45 + r54 + r56 + r57 + r59 + r61 + r63 + 2^{*}r73 + r79 + r81 + r87 + r99 + r103 + r109 + r119 + r125)$

$d[O]/dt = (-r140 - r2 - r8 - r11 - r13 - r15 - r20 - r30 - r46 - r52 - r56 - r57 - r68 - 2^{*}r70 - r72 - r76 - r86 - r92 - r96 - r118 - r128 - r138 + r1 + r7 + r12 + r14 + r16 + r19 + r29 + r45 + r51 + r55 + r58 + r67 + 2^{*}r69 + r71 + r75 + r85 + r91 + r95 + r117 + r127 + r137)$

$d[C2]/dt = (-r141 - r22 - r34 - r39 - r41 - r50 - r56 - r59 - r73 - r80 - r84 - r90 - r98 - r102 - r106 - r112 - r122 - r130 + r21 + r33 + r40 + r42 + r49 + r55 + r60 + r74 + r79 + r83 + r89 + r97 + r101 + r105 + r111 + r121 + r129)$

$d[CO]/dt = (-r142 - r2 - r10 - r12 - r18 - 2^{*}r24 - r27 - r29 - r31 - r33 \text{—} r36 - r40 - r45 - 2^{*}r47 - 2^{*}r49 - 2^{*}r51 - r53 - r55 - r57 - r59 - r61 - r63 - r65 - r67 - r84 - r108 - r116 - r134 + r1 + r9 + r11 + r17 + 2^{*}r23 + r28 + r30 + r32 + r34 + r35 + r39 + r46 + 2^{*}r48 + 2^{*}r50 + 2^{*}r52 + r54 + r56 + r58 + r60 + r62 + r64 + r66 + r68 + r83 + r107 + r115 + r133)$

$d[O2]/dt = (-r143 - r4 - r6 - r12 - r17 - r19 - r22 - r32 - r44 - r50 - r58 - r63 - r65 - r69 - r72 - r78 - r94 - r98 - 2^{*}r137 + r3 + r5 + r11 + r18 + r20 + r21 + r31 + r43 + r49 + r57 + r64 + r66 + r70 + r71 + r77 + r93 + r97 + 2^{*}r138)$

$d[C3]/dt = (-r144 - r79 - r86 - r94 - r108 - r114 - r124 - r132 + r80 + r85 + r93 + r107 + r113 + r123 + r131)$

$d[C2O]/dt = (-r145 - r32 - r35 - r37 - r40 - r52 - r54 - r60 - r61 - r78 - r82 - r96 - r106 - r124 - r136 + r31 + r36 + r38 + r39 + r51 + r53 + r59 + r62 + r77 + r81 + r95 + r105 + r123 + r135)$

$d[CO2]/dt = (-r146 - r1 - r3 - 2^{*}r5 - 2^{*}r7 - 2^{*}r9 - r11 - r13 - r15 - r17 - r19 - r21 - r23 - r25\ r27 - r29 - r31 - r33 - r35 - r37 - r39 - r41 - r43 - r90 - r114 + r2 + r4 + 2^{*}r6 + 2^{*}r8 + 2^{*}r10 + r12 + r14 + r16 + r18 + r20 + r22 + r24 + r26 + r28 + r30 + r32 + r34 + r36 + r38 + r40 + r42 + r44 + r89 + r113)$

$d[O3]/dt = (-r147 - r14 - r18 - r34 - r43 - r64 - r67 - r71 - r102 - r138 + r13 + r17 + r33 + r44 + r63 + r68 + r72 + r101 + r137)$

$d[C3O]/dt = (-r148 - r81 - r83 - r85 - r92 - r104 - r116 - r122 - r136 + r82 + r84 + r86 + r91 + r103 + r115 + r121 + r135)$

$d[C2O2]/dt = (-r149 - r6 - r26 - r30 - r36 - r42 - r48 - r62 - r76 - r88 - r95 - r97 - r112 - r132 + r5 + r25 + r29 + r35 + r41 + r47 + r61 + r75 + r87 + r96 + r98 + r111 + r131)$

$d[CO3]/dt = (-r150 - r10 - r16 - r20 - r44 - r66 - r68 - r100 + r9 + r15 + r19 + r43 + r65 + r67 + r99)$

$d[C4O]/dt = (-r151 - r103 - r105 - r107 - r118 - r120 - r134 + r104 + r106 + r108 + r117 + r119 + r133)$

$d[C3O2]/dt = (-r152 - r87 - r89 - r91 - r93 - r110 - r130 + r88 + r90 + r92 + r94 + r109 + r129)$

$d[C2O3]/dt = (-r153 - r8 - r28 - r38 - r75 - r77 - r99 - r101 + r7 + r27 + r37 + r76 + r78 + r100 + r102)$

$d[C5O]/dt = (-r154 - r119 - r121 - r123 - r128 + r120 + r122 + r124 + r127)$

$d[C4O2]/dt = (-r155 - r109 - r111 - r113 - r115 - r117 - r126 + r110 + r112 + r114 + r116 + r118 + r125)$

$d[C5O2]/dt = (-r156 - r125 - r127 - r129 - r131 - r133 - r135 + r126 + r128 + r130 + r132 + r134 + r136)$

The employed equations for the reaction rates are listed below, where $[i]$ is the column density in units of molecules per square centimeter, of a given species i, r_i is the reaction rates, k_i is the rate constant, k_des_i are the intrinsic desorption rate constant, L is the sample average thickness in units of centimeters, and $\Omega\_i = [i]/\Sigma[i]$ is the surface coverage of the species i as a function of time (a dimensionless quantity).

$r1 = k1\ ^{*}\ [CO2]$
$r2 = k2\ ^{*}\ [O]\ ^{*}\ [CO]\ /\ L$
$r3 = k3\ ^{*}\ [CO2]$
$r4 = k4\ ^{*}\ [C]\ ^{*}\ [O2]\ /\ L$
$r5 = k5\ ^{*}\ [CO2]\ ^{*}\ [CO2]\ /\ L$
$r6 = k6\ ^{*}\ [O2]\ ^{*}\ [C2O2]\ /\ L$
$r7 = k7\ ^{*}\ [CO2]\ ^{*}\ [CO2]\ /\ L$
$r8 = k8\ ^{*}\ [O]\ ^{*}\ [C2O3]\ /\ L$
$r9 = k9\ ^{*}\ [CO2]\ ^{*}\ [CO2]\ /\ L$
$r10 = k10\ ^{*}\ [CO]\ ^{*}\ [CO3]\ /\ L$
$r11 = k11\ ^{*}\ [O]\ ^{*}\ [CO2]\ /\ L$
$r12 = k12\ ^{*}\ [CO]\ ^{*}\ [O2]\ /\ L$
$r13 = k13\ ^{*}\ [O]\ ^{*}\ [CO2]\ /\ L$
$r14 = k14\ ^{*}\ [C]\ ^{*}\ [O3]\ /\ L$
$r15 = k15\ ^{*}\ [O]\ ^{*}\ [CO2]\ /\ L$
$r16 = k16\ ^{*}\ [CO3]$
$r17 = k17\ ^{*}\ [O2]\ ^{*}\ [CO2]\ /\ L$
$r18 = k18\ ^{*}\ [CO]\ ^{*}\ [O3]\ /\ L$
$r19 = k19\ ^{*}\ [O2]\ ^{*}\ [CO2]\ /\ L$
$r20 = k20\ ^{*}\ [O]\ ^{*}\ [CO3]\ /\ L$
$r21 = k21\ ^{*}\ [C]\ ^{*}\ [CO2]\ /\ L$
$r22 = k22\ ^{*}\ [C2]\ ^{*}\ [O2]\ /\ L$
$r23 = k23\ ^{*}\ [C]\ ^{*}\ [CO2]\ /\ L$
$r24 = k24\ ^{*}\ [CO]\ ^{*}\ [CO]\ /\ L$
$r25 = k25\ ^{*}\ [C]\ ^{*}\ [CO2]\ /\ L$
$r26 = k26\ ^{*}\ [C2O2]$
$r27 = k27\ ^{*}\ [CO]\ ^{*}\ [CO2]\ /\ L$
$r28 = k28\ ^{*}\ [C2O3]$
$r29 = k29\ ^{*}\ [CO]\ ^{*}\ [CO2]\ /\ L$
$r30 = k30\ ^{*}\ [O]\ ^{*}\ [C2O2]\ /\ L$
$r31 = k31\ ^{*}\ [CO]\ ^{*}\ [CO2]\ /\ L$
$r32 = k32\ ^{*}\ [O2]\ ^{*}\ [C2O]\ /\ L$

r33 = k33 * [CO] * [CO2] / L
r34 = k34 * [C2] * [O3] / L
r35 = k35 * [C2O] * [CO2] / L
r36 = k36 * [CO] * [C2O2] / L
r37 = k37 * [C2O] * [CO2] / L
r38 = k38 * [C] * [C2O3] / L
r39 = k39 * [C2] * [CO2] / L
r40 = k40 * [CO] * [C2O] / L
r41 = k41 * [C2] * [CO2] / L
r42 = k42 * [C] * [C2O2] / L
r43 = k43 * [CO2] * [O3] / L
r44 = k44 * [O2] * [CO3] / L
r45 = k45 * [CO]
r46 = k46 * [C] * [O] / L
r47 = k47 * [CO] * [CO] / L
r48 = k48 * [C2O2]
r49 = k49 * [CO] * [CO] / L
r50 = k50 * [C2] * [O2] / L
r51 = k51 * [CO] * [CO] / L
r52 = k52 * [O] * [C2O] / L
r53 = k53 * [C] * [CO] / L
r54 = k54 * [C2O]
r55 = k55 * [C] * [CO] / L
r56 = k56 * [O] * [C2] / L
r57 = k57 * [O] * [CO] / L
r58 = k58 * [C] * [O2] / L
r59 = k59 * [C2] * [CO] / L
r60 = k60 * [C] * [C2O] / L
r61 = k61 * [CO] * [C2O] / L
r62 = k62 * [C] * [C2O2] / L
r63 = k63 * [CO] * [O2] / L
r64 = k64 * [C] * [O3] / L
r65 = k65 * [CO] * [O2] / L
r66 = k66 * [CO3]
r67 = k67 * [CO] * [O3] / L
r68 = k68 * [O] * [CO3] / L
r69 = k69 * [O2]
r70 = k70 * [O] * [O] / L
r71 = k71 * [O3]
r72 = k72 * [O] * [O2] / L
r73 = k73 * [C2]
r74 = k74 * [C] * [C] / L
r75 = k75 * [C2O3]
r76 = k76 * [O] * [C2O2] / L
r77 = k77 * [C2O3]
r78 = k78 * [O2] * [C2O] / L
r79 = k79 * [C3]
r80 = k80 * [C] * [C2] / L
r81 = k81 * [C3O]
r82 = k82 * [C] * [C2O] / L
r83 = k83 * [C3O]
r84 = k84 * [C2] * [CO] / L
r85 = k85 * [C3O]
r86 = k86 * [O] * [C3] / L
r87 = k87 * [C3O2]
r88 = k88 * [C] * [C2O2] / L
r89 = k89 * [C3O2]
r90 = k90 * [C2] * [CO2] / L
r91 = k91 * [C3O2]
r92 = k92 * [O] * [C3O]/L
r93 = k93 * [C3O2]
r94 = k94 * [O2] * [C3] / L
r95 = k95 * [C2O2]
r96 = k96 * [O] * [C2O] / L
r97 = k97 * [C2O2]
r98 = k98 * [C2] * [O2] / L
r99 = k99 * [C2O3]
r100 = k100 * [C] * [CO3] /L
r101 = k101 * [C2O3]
r102 = k102 * [C2] * [O3] / L
r103 = k103 * [C4O]
r104 = k104 * [C] * [C3O] / L
r105 = k105 * [C4O]
r106 = k106 * [C2] * [C2O] / L
r107 = k107 * [C4O]
r108 = k108 * [CO] * [C3] / L
r109 = k109 * [C4O2]
r110 = k110 * [C] * [C3O2] / L
r111 = k111 * [C4O2]
r112 = k112 * [C2] * [C2O2] / L
r113 = k113 * [C4O2]
r114 = k114 * [C3] * [CO2] / L
r115 = k115 * [C4O2]
r116 = k116 * [CO] * [C3O] / L
r117 = k117 * [C4O2]
r118 = k118 * [O] * [C4O] / L
r119 = k119 * [C5O]
r120 = k120 * [C] * [C4O] / L
r121 = k121 * [C5O]
r122 = k122 * [C2] * [C3O] / L
r123 = k123 * [C5O]
r124 = k124 * [C3] * [C2O] / L
r125 = k125 * [C5O2]
r126 = k126 * [C] * [C4O2] / L
r127 = k127 * [C5O2]
r128 = k128 * [O] * [C5O] / L
r129 = k129 * [C5O2]
r130 = k130 * [C2] * [C3O2] / L
r131 = k131 * [C5O2]
r132 = k132 * [C3] * [C2O2] / L
r133 = k133 * [C5O2]
r134 = k134 * [CO] * [C4O] / L
r135 = k135 * [C5O2]
r136 = k136 * [C2O] * [C3O] / L
r137 = k137 * [O2] * [O2] / L
r138 = k138 * [O] * [O3] / L
r139 = k_des_C * Ω_C * [C]
r140 = k_des_O * Ω_O * [O]
r141 = k_des_C2 * Ω_C2 * [C2]
r142 = k_des_CO * Ω_CO * [CO]
r143 = k_des_O2 * Ω_O2 * [O2]
r144 = k_des_C3 * Ω_C3 * [C3]
r145 = k_des_C2O * Ω_C2O * [C2O]
r146 = k_des_CO2 * Ω_CO2 * [CO2]
r147 = k_des_O3 * Ω_O3 * [O3]
r148 = k_des_C3O * Ω_C3O * [C3O]
r149 = k_des_C2O2 * Ω_C2O2 * [C2O2]
r150 = k_des_CO3 * Ω_CO3 * [CO3]
r151 = k_des_C4O * Ω_C4O * [C4O]
r152 = k_des_C3O2 * Ω_C3O2 * [C3O2]
r153 = k_des_C2O3 * Ω_C2O3 * [C2O3]
r154 = k_des_C5O * Ω_C5O * [C5O]
r155 = k_des_C4O2 * Ω_C4O2 * [C4O2]
r156 = k_des_C5O2 * Ω_C5O2 * [C5O2]

Appendix C
Comparison between the Phase 1 and Phase 2 Calculations

Figure C1 presents, for comparison purposes, the ERCs' values of the final solution obtained at phase 1 (precursor best-fit model), which consider the ordering hypothesis for the ERCs based on thermochemistry data and the final solution obtained at phase 2 (the best-fit model) at which the calculation starts considering the phase 1 solution and not considering any previous ordering hypothesis for the ERCs. Phase 1 and phase 2 are represented by the black (small symbols) and blue colors, respectively. Panels (a)–(c) indicate the ERCs for the intrinsic desorption, direct, and bimolecular reactions, respectively. The average values for phase 2 (final best-fit model) are indicated near the horizontal blue dashed line.

In Figure C1 we observe that some ERCs present considerable changes between these two sets of solutions (from phase 1 to phase 2) indicating that these reactions do not strictly follow the ordering hypothesis considered in the first phase. The vertical lines indicate the intensity of individual variations on the ERCs and its colors indicate it increases (blue) or decrease (red) from phase 1 to phase 2. A small increase in the ERCs was observed for k21, k47, k93, k125, k143, k144, and a large increase was observed for k13 and k68. The values of k24, k141, k147, k148, and k155 presented a small decrease, and k46, k70, k74, and k80 presented a large decrease compared to the best-fit solution of these two phases. Further publication might explore this finding from a deeper physico-chemical point of view.

It is worth noting that the current methodology also increases the accuracy of the final solution since the summed χ^2 function of these two sets of solutions slightly decreases from 0.88 (phase 1) to 0.79 (phase 2; the best-fit model).

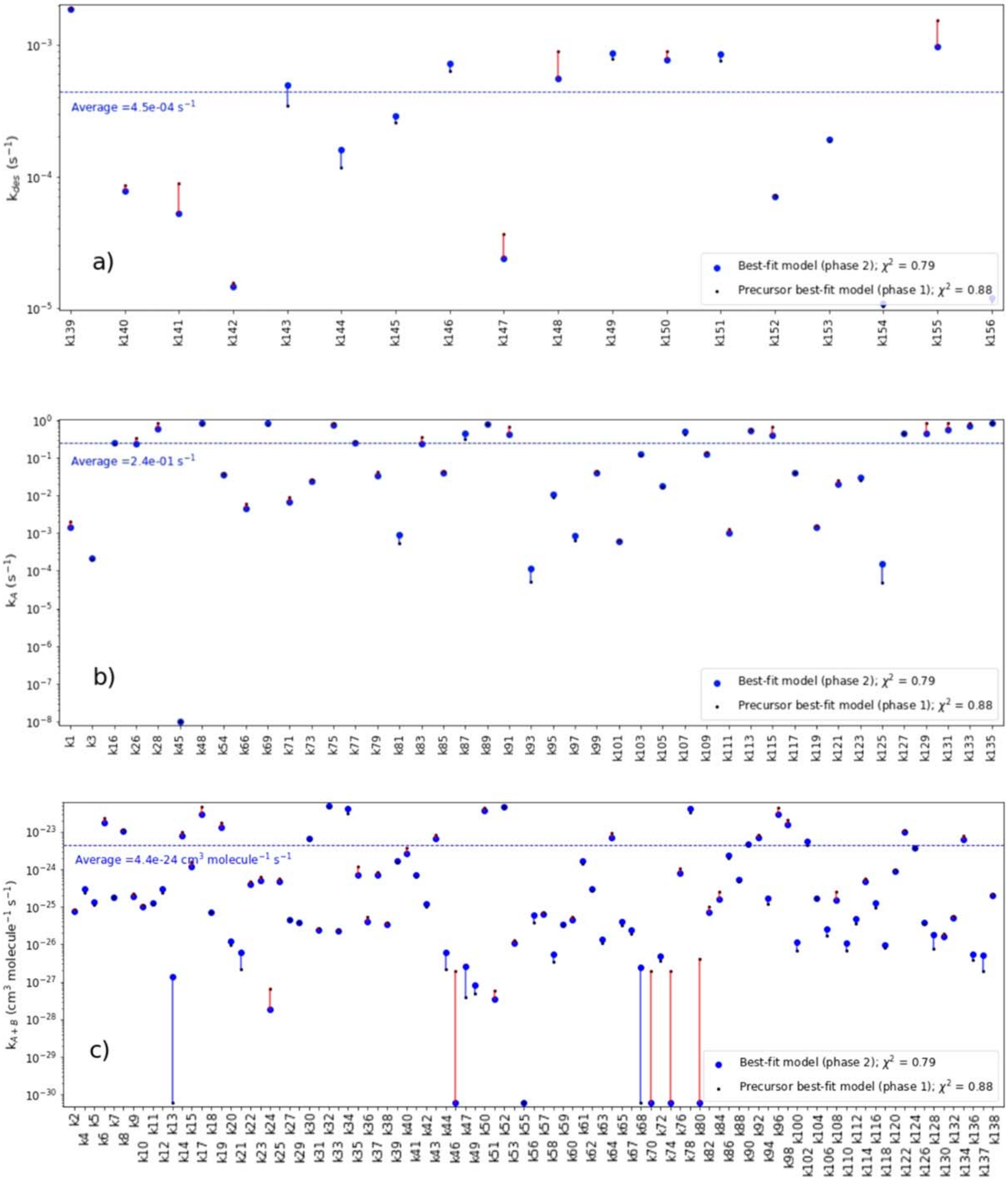

Figure C1. Comparisons between the values of ERCs obtained in the best-fit model of phase 1 (with ERCs' ordering hypothesis) and the final best-fit model of phase 2 (starting from the phase 1 solution and not considering any previous ordering hypothesis for the ERCs). Phase 1 and phase 2 are represented by the black (small symbols) and blue colors, respectively. Panel (a)–(c) indicate the ERCs for the intrinsic desorption, direct and bimolecular reactions, respectively. Verticals lines indicate the intensity of individual variations on the ERCs and its colors indicate it increases (blue) or decreases (red) from phase 1 to phase 2. The average values for phase 2 (final best-fit model) are indicated near the horizontal blue dashed line.

ORCID iDs

S. Pilling https://orcid.org/0000-0002-6321-3666
G. A. Carvalho https://orcid.org/0000-0001-8718-6925
B. R. L. Galvão https://orcid.org/0000-0002-4184-2437

References

Ahrens, C., Meraviglia, H., & Bennett, C. 2022, Geosc, 12, 51
Alves, E., Franco, M. P., Pilling, S., Machado, F. B., & Spada, R. F. 2021, J. Mol. Model., 27, 264
Andrade, D. P. P., Boechat-Roberty, H. M., da Silveira, E. F., et al. 2008, JChPh, 112, 11954
Atkins, P. 1998, Physical Chemistry (6th ed.; New York: Freeman), 825
Ballering, N. P., Cleeves, L. I., & Anderson, D. E. 2021, ApJ, 920, 115
Beaulieu, J. P., Bennett, D. P., Fouqué, P., et al. 2006, Natur, 439, 437
Bennett, C. J., Jamieson, C. S., & Kaiser, R. I. 2010, PCCP, 12, 4032
Bennett, C. J., Jamieson, C. S., & Kaiser, R. I. 2009, PCCP, 11, 4210
Bennett, C. J., Jamieson, C., Mebel, M., & Kaiser, R. I. 2004, PCCP, 6, 735
Bertrand, T., & Forget, F. 2016, Natur, 540, 86
Boduch, P., Dartois, E., de Barros, A. L., et al. 2015, JPhCS, 629, 012008
Boogert, A. C. A., Gerakines, P. A., & Whittet, D. C. B. 2015, ARA&A, 53, 541

Bossa, J. B., Isokoski, K., Paardekooper, D. M., et al. 2014, A&A, 561, A136

Bossa, J. B., Paardekooper, D. M., Isokoski, K., & Linnartz, H. 2015, PCCP, 17, 17346

Burschka, M. A. 1997, A Diffusion-limited Reaction. In Stochastic Dynamics (Berlin: Springer), 88

Carvalho, G. A., Pilling, S., & Galvão, B. R. 2022, MNRAS, 515, 3760

Cecchi-Pestellini, C., & Aiello, S. 1992, MNRAS, 258, 125

Cernicharo, J., Goicoechea, J. R., & Caux, E. 2000, ApJL, 534, L199

Cernicharo, J., Agúndez, M., Cabezas, C., et al. 2021, A&A, 656, L21

Chang, R. 2005, Physical Chemistry for the Biosciences (Sausalito, CA: Univ. Science Books)

Ciaravella, A., Chen, Y.-J., Cecchi-Pestellini, C., et al. 2016, ApJ, 819, 38

Ciaravella, A., Jiménez-Escobar, A., Caro, G. M., et al. 2012, ApJL, 746, L1

Cottin, H., Moore, M. H., & Bénilan, Y. 2003, ApJ, 590, 874

Crovisier, J., Encrenaz, T., & Combes, M. 1991, Natur, 353, 610

Cuppen, H. M., Walsh, C., Lamberts, T., et al. 2017, SSRv, 212, 1

Dartois, E., Chabot, M., Barkach, T. I., et al. 2021, A&A, 647, A177

de Araujo Vasconcelos, F., Pilling, S., Rocha, W. R. M., Rothard, H., & Boduch, P. 2017, ApJ, 850, 174

de Barros, A. L. F., Seperuelo Duarte, E., Farenzena, L.S., et al. 2011, NIMPB, 269, 852

de Barros, A. L. F., Mejía, C., Seperuelo Duarte, E., et al. 2022, MNRAS, 511, 2491

Ehrenfreund, P., & Cami, J. 2010, Cold Spring Harbor Perspect. Biol., 2, a002097

Eistrup, C., & Henning, T. 2022, A&A, 667, A160

Gambi, A., Giumanini, A. G., & Strazzolini, P. 2001, J. Mol. Struct.: THEOCHEM, 536, 9

Gerakines, P. A., Schutte, W. A., & Ehrenfreund, P. 1996, A&A, 312, 289

Gibb, E. L., Whittet, D. C. B., Boogert, A. C. A., & Tielens, A. G. G. M. 2004, ApJS, 151, 35

Gredel, R., Lepp, S., Dalgarno, A., & Herbst, E. 1989, ApJ, 347, 289

Guélin, M., & Cernicharo, J. 2022, FrASS, 9, 787567

Heays, A. N., Bosman, A. V., & Van Dishoeck, E. F. 2017, A&A, 602, A105

Herbst, E., & van Dishoeck, E. F. 2009, ARA&A, 47, 427

Huang, C.-H., Ciaravella, A., Cecchi-Pestellini, C., et al. 2020, ApJ, 889, 57

Huntress, W. T., Allen, M., & Delitsky, M. 1991, Natur, 352, 316

Husain, D., & Young, A. N. 1975, J. Chem. Soc., Faraday Trans. 2, 71, 525

Jamieson, C. S., Mebel, A. M., & Kaiser, R. I. 2006, ApJS, 163, 184

Jiménez-Escobar, A., Chen, Y. J., Ciaravella, A., et al. 2016, ApJ, 820, 25

Konkoli, Z. 2009, Electronic Proceedings in Theoretical Computer Science, 9, 98

Lacy, J. H., Baas, F., Allamandola, L. J., et al. 1984, ApJ, 276, 533

Lellouch, E., de Bergh, C., Sicardy, B., Ferron, S., & Käuf, H.-U. 2010, A&A, 512, L8

Lewars, E. G. 2008, Modeling Marvels (Dordrecht: Springer), 131

Lin, H. W., Lee, C. H., Gerdes, D. W., et al. 2020, ApJL, 889, L30

Loeffler, M. J., Baratta, G. A., Palumbo, M. E., Strazzulla, G., & Baragiola, R. A. 2005, A&A, 435, 587

Mainitz, M., Anders, C., & Urbassek, H. M. 2016, A&A, 592, A35

Mallard, W. G., Westley, F., Herron, J. T., et al. 2004, NIST Chemical Kinetics Database v6.0, https://kinetics.nist.gov/

McElroy, D., Walsh, C., Markwick, A. J., et al. 2013, A&A, 550, A36

Mookerjea, B., Giesen, T., Stutzki, J., et al. 2010, A&A, 521, L13

Neese, F., Wennmohs, F., Becker, U., & Riplinger, C. 2020, JChPh, 152, 224108

Öberg, K. I., Boogert, A. A., Pontoppidan, K. M., et al. 2011, ApJ, 740, 109

Ohishi, M., Ishikawa, S., Yamada, C., et al. 1991, ApJL, 380, L39

Palumbo, M. E., Leto, P., Siringo, C., & Trigilio, C. 2008, ApJ, 685, 1033

Pilling, S., Andrade, D. P. P., Neto, A. C., et al. 2009, JPCA, 113, 11161

Pilling, S., & Bonfim, V. S. 2020, RSCAd, 10, 5328

Pilling, S., Duarte, E. S., da Silveira, E. F., et al. 2010b, A&A, 509, A87

Pilling, S., Andrade, D. P. P., do Nascimento, E. M., et al. 2011, MNRAS, 411, 2214

Pilling, S., Duarte, E. S., Domaracka, A., et al. 2010a, A&A, 523, A77

Pilling, S., Carvalho, G. A., & Rocha, W. R. 2022, ApJ, 925, 147

Pilling, S., Rocha, W. R. M., Carvalho, G. A., & de Abreu, H. A. 2023, ASR, 71, 5466

Rice, S. A. 1985, in Comprehensive Chemical Kinetics. Diffusion-limited Reactions, ed. C. H. Bamfrod, C. F. H. Tipper, & R. G. Compton, 25 (Amsterdam: Elsevier)

Rocha, W. R. M., Voitke, P., Pillind, S., et al. 2023, A&A, 673, A70

Ruscic, B., & Bross, D. H. 2020, Active Thermochemical Tables (ATcT), https://atct.anl.gov/

Ruscic, B., Pinzon, R. E., Morton, M. L., et al. 2004, JPCA, 108, 9979

Ruscic, B., Pinzon, R. E., von Laszewski, G., et al. 2005, JPhCS, 16, 561

Satorre, M., Palumbo, M., & Strazzulla, G. 2000, Ap&SS, 274, 643

Seperuelo Duarte, E., Boduch, P., Rothard, et al. 2009, A&A, 502, 599

Seperuelo Duarte, E., Domaracka, A., Boduch, P., et al. 2010, A&A, 512, A71

Shoup, D., Lipari, G., & Szabo, A. 1981, BpJ, 36, 697

Sicilia, D., Ioppolo, S., Vindigni, T., Baratta, G. A., & Palumbo, M. E. 2012, A&A, 543, A155

Souza, S. P., & Lutz, B. L. 1977, ApJL, 216, L49

Trottier, A., & Brooks, R. L. 2004, ApJ, 612, 1214

Urso, R. G., Palumbo, M. E., Ceccarelli, C., et al. 2019, A&A, 628, A72

van Dishoeck, E. F. 1988, in Rate Coefficients in Astrochemistry, ed. T. J. Millar & D. A. Williams (Dordrecht: Springer), 49

van Dishoeck, E. F., Jonkheid, B., & van Hemert, M. C. 2006, FaDi, 133, 231

Wang, H. Y., Lu, X., Huang, R. B., & Zheng, L. S. 2002, JMoSt, 593, 187

Whittet, D. C. B., Gerakines, P. A., Tielens, G. G. M., et al. 1998, ApJL, 498, L159